

Temperature Effects
in
Optical Fiber Dispersion Compensation
Modules

by

Mikhail Shenouda

A thesis
presented to the University of Waterloo
in fulfillment of the
thesis requirement for the degree of
Master of Science
in
Physics

Waterloo, Ontario, Canada, 2013

©Mikhail Shenouda 2013

AUTHOR'S DECLARATION

I hereby declare that I am the sole author of this thesis. This is a true copy of the thesis, including any required final revisions, as accepted by my examiners.

I understand that my thesis may be made electronically available to the public.

Abstract

This thesis presents the results for the temperature variation of the Differential Group Delay (DGD) measurements of a Dispersion Compensation Module (DCM) and interprets the results with a theoretical DGD model based on glass viscoelastic properties and estimated values of some of glass parameters. The results of our analysis demonstrate the existence of long birefringence relaxation times on the order of many hours in response to temperature changes. These results could be of significance in interpreting the behavior of optical fiber systems.

Acknowledgements

I would like to thank Prof. David Yevick (my supervisor) for his guidance and the enlightening conversations we had during my master's program. I also would like to acknowledge George Soliman (a dear friend and a teammate) for his help and advice. I also thank Michael Gad for pointing out this master's opportunity for me.

I would like to thank our secretary staff for being always available for administrative inquiries and guidance.

Dedication

I dedicate this master's thesis to my family, especially my parents, and to their constant support to me through my life.

Table of Contents

AUTHOR'S DECLARATION.....	ii
Abstract.....	iii
Acknowledgements.....	iv
Dedication.....	v
Table of Contents.....	vi
List of Figures.....	viii
List of Tables.....	xi
List of Acronyms.....	xii
Chapter 1 Theoretical and Mathematical Introduction to Polarization and Differential Group Delay (DGD) in Fibers.....	1
1.1 Overview.....	1
1.2 Light polarization [2].....	2
1.2.1 Jones mathematical representation.....	2
1.2.2 Stokes parameters representation.....	2
1.2.3 Jones Matrix & Rotation matrix.....	3
1.2.4 Principal states of polarization (PSP).....	6
1.2.5 PMD vector and DGD.....	7
1.2.6 Differential rotations.....	8
1.3 Long fiber cable analysis, concatenated sections model [2].....	9
1.4 Resultant PMD vector of concatenated sections [2].....	9
1.5 Measuring DGD in lab environment.....	12
Chapter 2 Relaxation of stress and strain in fibers.....	14
2.1 Overview.....	14
2.2 Viscoelasticity of glass.....	15
2.3 Mechanical constants of glass.....	17
2.3.1 Young's Modulus of glass.....	17
2.3.2 Viscosity and Volume Viscosity.....	18
2.4 Optical properties of glass.....	19
2.4.1 Refractive index and temperature [10].....	19

Chapter 3 Previous work and literature review	22
3.1 Temperature measurements for different fiber based optical components.....	22
3.1.1 Time evolution measurements on installed fibers	22
3.1.2 Dispersion compensation modules (DCMs) under temperature variations	25
3.2 Mathematical models of mechanical and temperature effects on birefringence	26
3.2.1 Birefringence due to geometrical deformation	26
3.2.2 Birefringence due to built-in stresses [20].....	28
3.2.3 Birefringence due to bends [21]	30
3.2.4 Birefringence due to bends under tension [22].....	31
3.2.5 Birefringence due to twists [23]	33
Chapter 4 Dispersion Compensation Modules (DCMs) behavior under temperature variations	34
4.1 THE EXPERIMENT	34
4.1.1 Setup Description	34
4.1.2 Experiment Procedure	34
4.2 Results	35
4.2.1 DCM under room temperature effect	35
4.2.2 DCM's DGD vs. Temperature.....	36
4.2.3 Hysteresis and temperature spans.....	38
4.2.4 DGD relaxation with time	42
Chapter 5 Modeling the DCM.....	44
5.1 Fiber-based DCM's strain model	44
5.2 Physical parameters and mathematical equations.....	46
5.2.1 Single section general model.....	46
5.2.2 Total DGD of the system.....	49
5.3 Numerical results.....	50
5.4 Conclusion.....	52
Appendix A Matlab code to plot measured data and prepare it for simulation	53
Appendix B Matlab model	56
Bibliography.....	61

List of Figures

Figure 1.1	Poincaré sphere showing special cases of polarizations [2].....	3
Figure 1.2	Polarization transformation on the Poincaré sphere. P and P' are the input and output SOPs respectively. Γ represents the rotation angle γ . [2].	5
Figure 1.3	Polarization transformation on the Poincaré sphere. Q and Q' are the output SOPs at ω_0 and $\omega_0 + \Delta\omega$, respectively, for the same input SOP. $\tau\Delta\omega$ represents the rotation angle γ around the slow PSP. [2].	7
Figure 1.4	A long segment of fiber is represented by a series of birefringent elements. The slow axis of adjacent birefringent elements is arbitrary orientated. [2].....	9
Figure 1.5	Linear input output relationship of a birefringent fiber system. [2].....	9
Figure 1.6	Concatenation of two birefringent sections. [2].....	10
Figure 1.7	A diagram showing a birefringent section and the reference x and y axis, the fast and slow mode axis and the angle Ψ between them. [2].....	10
Figure 2.1	Coordinate system and components of stress [6].....	14
Figure 2.2	A Voigt element in series with a spring to model the viscoelasticity of glass [6]. ..	16
Figure 2.3	Some mechanical constants of silica glass [7].	17
Figure 2.4	Mechanical constants of different types of glass [8].....	17
Figure 2.5	Mazurin et al. - viscosity measurements versus temperature for different types of glass [6] (pages 149-150).....	18
Figure 2.6	Zijlstra's - viscosity measurements versus temperature for different types of glass [6] (pages 149-151).....	19
Figure 3.1	“Time evolution of the normalized stokes vector (left side graph) and that of the DGD (right side graph) of the first measurement (sunset = *, sunrise = **)” [11].....	22
Figure 3.2	“Time evolution of the normalized stokes vector (left side graph) and that of the DGD (right side graph) of the second measurement (sunset = *, sunrise = **)” [11].....	23
Figure 3.3	“Time evolution of PMD (upper curve), and temperature at the outside of the 36 km fiber spool (lower curve)” [13]	23
Figure 3.4	“Time evolution of PMD (upper curves), and temperature measured a meter above ground (lower curves) for the 48.8 Km buried cable (left side curves) and the 96 Km aerial cable (right side curves)” [13]	24
Figure 3.5	“Changes of Δ DGD for 3 wavelengths, $\lambda=1529.5 \mu\text{m}$ (●), $\lambda=1533.5 \mu\text{m}$ (○) and $\lambda=1556.5 \mu\text{m}$ (▼), as a function of time (left axis). The thick dotted lines (●) is the ambient temperature (right axis)” [14]	24

Figure 3.6	Same data as previous figure but presented as a function of temperature ($\lambda=1529.5 \mu\text{m}$ (●), $\lambda=1533.5 \mu\text{m}$ (○) and $\lambda=1556.5 \mu\text{m}$ (▼)) [14].....	24
Figure 3.7	“Plot similar to Figure 3.6, but with a data span over 3 weeks of measurements” [14] 25	
Figure 3.8	“Grey-scale plots of the DGD spectra as a function of time during 6 temperature cycles (far right side). a) DCM#1 b)DCM#2” [15].....	25
Figure 3.9	“a) Grey-scale plots of the DGD spectra as a function of time during thermal shock, with temperature profile to the right. b) DGD spectra before (black) temperature cycles and after the thermal shock (dark blue) and after two temperature cycles (light blue)” [15].....	26
Figure 3.10	Elliptical core fiber’s diagram.....	27
Figure 3.11	“Cross section of fibers with elliptical structure. (a) Round core in an elliptical inner cladding. (b) Elliptical core in a round cladding.” [20].....	28
Figure 3.12	“Frequency dependence of the three kinds of linear birefringence” [20].....	29
Figure 3.13	“Geometry of a bent fiber” [21]	30
Figure 3.14	“Bending birefringence of single-mode silica fibers. The solid line represents the calculated birefringence (3.7). The points are measurements at 0.633 and $0.676 \mu\text{m}$ using three fibers of different origins. ($\kappa=1/R$)” [21].....	31
Figure 3.15	“Geometry of a tension-coiled fiber” [22].....	32
Figure 3.16	“Tension-coiled birefringence β_{tc} of single-mode fibers. The solid lines represent the calculated birefringence. Measurements for $\lambda = 0.633 \mu\text{m}$ are indicated by the dots. ($\kappa=1/R$)” [22]...	32
Figure 4.1	Setup block diagram, showing signals and laser flows.	34
Figure 4.2	DGD evolution in room temperature for 76.5 hours	35
Figure 4.3	DGD vs. Room Temperature.....	36
Figure 4.4	Reproducible curves under same circumstances	36
Figure 4.5	Irreproducible curves of DGD vs. Temperature at different Temperatures ranges ..	37
Figure 4.6	Irreproducible curves of DGD and Temperature different settling times.....	38
Figure 4.7.1	The DGD measured when heating (Solid lines) and cooling (Dotted lines) the DCM from different starting temperatures to 32°C	39
Figure 4.7.2	Divergence between heating and cooling measurements for the curves in the above figure.	39
Figure 4.8.1	Heating (Solid lines) and cooling (Dotted lines) measurements with a minimum of 26°C and maximum variable temperatures.	40

Figure 4.8.2	Divergence between heating and cooling measurements for the curves in the above figure.	40
Figure 4.9.1	Heating (Solid lines) and cooling (Dotted lines) measurements with variable maximum and minimum temperatures.	41
Figure 4.9.2	Divergence between heating and cooling measurements for the curves in the above figure.	41
Figure 4.10	DGD vs. Time at different temperatures (8 hours per temperature)	42
Figure 4.11	DGD vs. Time during the second temperature cycle displayed in the previous figure.	43
Figure 5.1	Averaged measured DGD (red curves) and Simulated DGD (blue curves) versus Temperature	50
Figure 5.2	DGD (Measured and Simulated) and Temperature versus Time	51
Figure 5.3	A zoomed view on the second heating cycle	51

List of Tables

Table 2-1 "Refractive index vs temperature, fused silica, Corning code 7940, ultraviolet grade" [10]	20
Table 2-2 "Refractive index vs temperature, alumino-silicate glass, Corning code 1723" [10]	20
Table 2-3 "Refractive index vs temperature, Vycor Corning code 7913, optical grade" [10]	21
Table 5-1 Physical parameters characterizing the fiber-based DCM (SI units)	46
Table 5-2 Relations used to obtain fiber parameters	47
Table 5-3 Mathematical model of the fiber-based DCM.....	47

List of Acronyms

- DCM: Dispersion Compensation Module
- DGD: Differential Group Delay
- PMD: Polarization Mode Dispersion
- PSP: Principal State of Polarization
- SI units: International System of Units
- SOP: State Of Polarization

Chapter 1

Theoretical and Mathematical Introduction to Polarization and Differential Group Delay (DGD) in Fibers

1.1 Overview

Optical communications is increasingly dominating telecommunication systems; as a result of its ability to provide large data rates in response to increased bandwidth demand. Since optical fibers have been employed as a transmission medium, high data rates over long fiber spans require efficient and high-performance distributed amplification and dispersion compensation modules, optimally in conjunction with low loss and dispersion fibers. However, optical cables laid in the ground are susceptible to long term changes caused by the surrounding environment while optical components; like filters, amplifiers and DCM's; are subject to daily temperature changes, causing their parameters to fluctuate frequently and hence affecting the link stability.

Dispersion, which leads to pulse broadening, is classified as, firstly, *Material Dispersion*, which results when the refractive index of the dielectric medium varies with the optical frequency of the pulse and therefore is associated with bulk glass. *Waveguide Dispersion* results from the change in the propagation constant with optical frequency while additionally *Multimode Dispersion* occurs when a waveguide supports multiple modes, which correspond to several classical ray paths, with different angles of propagation through the optical fiber. The effect of dispersion is therefore to broaden a pulse at the output of the fiber.

Polarization Mode Dispersion (PMD) results from the dependence of the propagation constant on polarization resulting from the small but unavoidable presence of birefringence in optical fibers. In birefringent media light experiences slightly different effective refractive indices according to its polarization and propagation direction. While a perfectly circular, stress-free fiber is not birefringent; as a result of the manufacturing process, fibers possess slight elliptical core distortions. Fibers also encounter mechanical stresses in both the manufacturing process and that of cabling, due to twists and bends. Since PMD not only affects the amplitude but also the phase of the signal, it must be appropriately reduced or compensated in optical systems, especially coherent ones.

PMD, which can be influenced by changes in birefringence generated by twists, and bends and transverse forces and temperature variations, causes a stochastic distortion of the output signal. This results in fading at the receiver's end for both coherent and direct detection systems [1]. Consequently, while PMD can be compensated through either optical or electronic compensation using signal processing techniques, Further PMD compensation techniques should optimally be able to detect temporal changes, if not anticipate them, to maintain the stability of the system and avoid fading.

This chapter discusses mathematical representations of in fiber polarizations and related calculation methods.

1.2 Light polarization [2]

An electromagnetic wave possesses two transverse polarization directions. This section discusses the Jones and Stokes formalism for polarization in fibers as well as presents a mathematical description of PMD.

1.2.1 Jones mathematical representation

In the Jones representation, an optical wave is described by a column vector

$$\mathbf{J} = \begin{bmatrix} A_x e^{i\delta_x} \\ A_y e^{i\delta_y} \end{bmatrix} \quad (1.1)$$

where A_x and A_y are the electric field amplitudes of the corresponding axis noted by the subscript; while δ is the phase corresponding to each electric field component. If \mathbf{J} is normalized to unit power, Eq.(1.1) can be rewritten as

$$\mathbf{J} = \begin{bmatrix} \cos \Psi \\ e^{i\delta} \sin \Psi \end{bmatrix} \quad (1.2)$$

in which δ is the difference between δ_y and δ_x and Ψ is the azimuth angle of the resultant electric field with respect to the x axis ($\Psi = \cos^{-1}\left(\frac{A_y}{A_x}\right)$). Here \mathbf{J} in equation (1.2) is a unitary vector representing only the polarization profile ($Power = \mathbf{J}^* \mathbf{J}^\dagger = 1$).

1.2.2 Stokes parameters representation

The state of polarization is also often represented by the Stokes parameters.

$$\begin{aligned} S_0 &= \langle\langle A_x^2 + A_y^2 \rangle\rangle \\ S_1 &= \langle\langle A_x^2 - A_y^2 \rangle\rangle \\ S_2 &= 2 \langle\langle A_x A_y \cos \delta \rangle\rangle \\ S_3 &= 2 \langle\langle A_x A_y \sin \delta \rangle\rangle \end{aligned} \quad (1.3)$$

S_0 is proportional to the optical power while $\langle\langle \quad \rangle\rangle$ represents the time average. For fully polarized light, the parameters can be normalized as below,

$$\begin{aligned} S_0 &= 1 \\ S_1 &= \cos 2\Psi \\ S_2 &= \sin 2\Psi \cos \delta \\ S_3 &= \sin 2\Psi \sin \delta \end{aligned} \quad (1.4)$$

so that S_1 , S_2 and S_3 , are sufficient to describe the polarization state of a fully polarized wave.

Plotting these parameters on orthogonal axes yields the Poincaré sphere (Figure 1.1) which is particularly convenient for displaying the evolution of polarization with wavelength or time. On the sphere, all polarization states on the equator are linearly polarized, while the states at the poles are circularly polarized and elliptically polarized elsewhere. Plotting states of polarizations on the Poincaré sphere yields a smooth curve for the polarization evolution of either the output at a single wavelength or the evolution of polarization with wavelength, as will be demonstrated later.

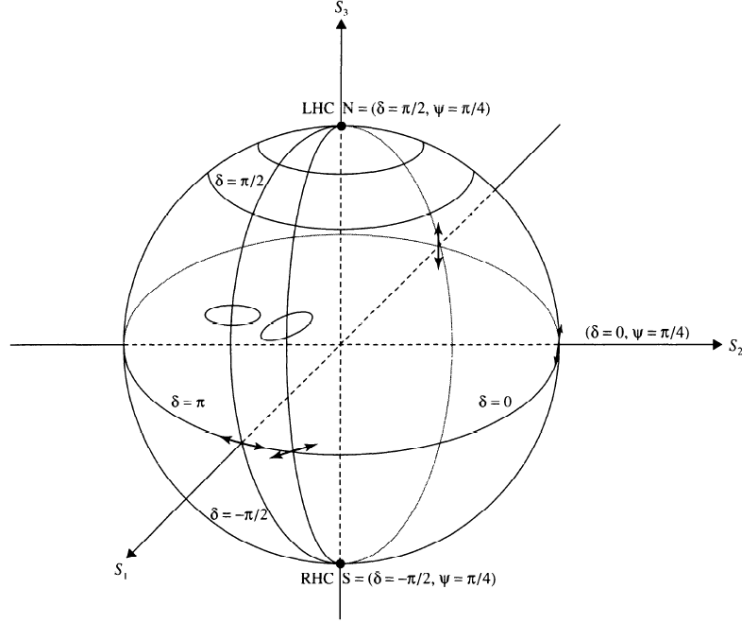


Figure 1.1 Poincaré sphere showing special cases of polarizations [2].

1.2.3 Jones Matrix & Rotation matrix

The Jones matrix is a 2×2 matrix in the Jones representation (Noted as U) while the Rotation Matrix is a 3×3 matrix in the Stokes parameter representation (Noted as R). These matrices model and relate the input polarization to the output polarization in any birefringent system. Thus in the Jones Matrix representation

$$\begin{bmatrix} \cos \Psi^v \\ e^{i\delta^v} \sin \Psi^v \end{bmatrix} = U \begin{bmatrix} \cos \Psi^s \\ e^{i\delta^s} \sin \Psi^s \end{bmatrix} \quad (1.5)$$

$$|v\rangle = U |s\rangle$$

Here $|v\rangle$ and $|s\rangle$ represent the Jones vectors of the output polarization and input polarization respectively. U is a unitary unimodular matrix; that follows

$$U = \begin{bmatrix} a & b \\ -b^* & a^* \end{bmatrix} \quad (1.6)$$

with $|a|^2 + |b|^2 = 1$. In the Stokes representation,

$$\begin{bmatrix} s_1^v \\ s_2^v \\ s_3^v \end{bmatrix} = R \begin{bmatrix} s_1^s \\ s_2^s \\ s_3^s \end{bmatrix} \quad (1.7)$$

$$\mathbf{v} = R\mathbf{s}$$

in which \mathbf{v} and \mathbf{s} are the three-dimensional Stokes vectors of the output polarization and input polarization respectively. The Pauli spin vector $\boldsymbol{\sigma}$ components are employed to transform a Jones matrix or vector to Stokes' space.

$$\boldsymbol{\sigma} = \begin{bmatrix} \sigma_1 \\ \sigma_2 \\ \sigma_3 \end{bmatrix} \quad (1.8)$$

and

$$\sigma_1 = \begin{bmatrix} 1 & 0 \\ 0 & -1 \end{bmatrix}, \sigma_2 = \begin{bmatrix} 0 & 1 \\ 1 & 0 \end{bmatrix}, \sigma_3 = \begin{bmatrix} 0 & -i \\ i & 0 \end{bmatrix} \quad (1.9)$$

Hence

$$\mathbf{s} = \langle s | \boldsymbol{\sigma} | s \rangle, \mathbf{v} = \langle v | \boldsymbol{\sigma} | v \rangle \quad (1.10)$$

which is an abbreviated notation for

$$s_1 = \langle s | \sigma_1 | s \rangle, s_2 = \langle s | \sigma_2 | s \rangle, s_3 = \langle s | \sigma_3 | s \rangle \quad (1.11)$$

Consequently the relation between R and U is given by

$$\begin{aligned} \mathbf{v} &= R\mathbf{s} = R \langle s | \boldsymbol{\sigma} | s \rangle = \langle s | R\boldsymbol{\sigma} | s \rangle \\ \mathbf{v} &= \langle v | \boldsymbol{\sigma} | v \rangle = \langle s | U^\dagger \boldsymbol{\sigma} U | s \rangle \end{aligned} \quad (1.12)$$

From the upper set of equations

$$R\boldsymbol{\sigma} = U^\dagger \boldsymbol{\sigma} U \quad (1.13)$$

where “ \dagger ” represents the Hermitian conjugate.

For every Jones or rotation matrix representing a birefringent section two input polarizations maintain the same polarization at the output. These input states obey the relations

$$|v\rangle = U|r\rangle = e^{-i\frac{\gamma}{2}}|r\rangle \quad \text{and} \quad |v\rangle = U|r_-\rangle = e^{+i\frac{\gamma}{2}}|r_-\rangle \quad (1.14)$$

Here the polarization states of the slow and fast modes $|r\rangle$ and $|r_-\rangle$, respectively, are the eigenvectors of the matrix U with eigenvalues $e^{-i\frac{\gamma}{2}}$ and $e^{+i\frac{\gamma}{2}}$; where $-i\frac{\gamma}{2}$ and $+i\frac{\gamma}{2}$ represent the difference in phase between the input and output wave. The quantity γ also represents the rotation angle between the input SOP (State Of Polarization) and the output SOP around the slow mode axis (also called the rotation axis) on the Poincaré sphere; that is “ \mathbf{r} ” in terms of Stokes parameters, calculated following the example of equation(1.10).

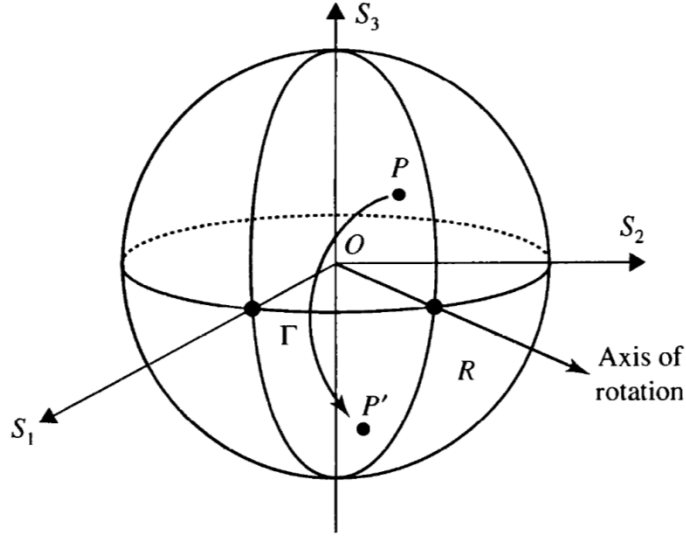


Figure 1.2 Polarization transformation on the Poincaré sphere. P and P' are the input and output SOPs respectively. Γ represents the rotation angle γ . [2].

Expressing U in terms of its eigenvectors and eigenvalues,

$$U = e^{-i\frac{\gamma}{2}}|r\rangle\langle r| + e^{+i\frac{\gamma}{2}}|r_-\rangle\langle r_-| \quad (1.15)$$

where [3]

$$|r\rangle\langle r| = \frac{1}{2}(I + \mathbf{r} \cdot \boldsymbol{\sigma}) \quad (1.16)$$

The two previous equations yield

$$U = \cos\left(\frac{\gamma}{2}\right)I - i \sin\left(\frac{\gamma}{2}\right)\mathbf{r} \cdot \boldsymbol{\sigma} \quad (1.17)$$

Substituting equation (1.17) in (1.13) leads to, after some algebra,

$$R = \mathbf{r}\mathbf{r} + \sin(\gamma)\mathbf{r} \times -\cos(\gamma)\mathbf{r} \times \mathbf{r} \times \quad (1.18)$$

or in terms of components

$$R = \begin{bmatrix} r_1 r_1 & r_1 r_3 & r_1 r_3 \\ r_2 r_1 & r_2 r_2 & r_2 r_3 \\ r_3 r_1 & r_3 r_2 & r_3 r_3 \end{bmatrix} + \sin(\gamma) \begin{bmatrix} 0 & -r_3 & r_2 \\ r_3 & 0 & -r_1 \\ -r_2 & r_1 & 0 \end{bmatrix} - \cos(\gamma) \begin{bmatrix} r_1 r_1 - 1 & r_1 r_2 & r_1 r_3 \\ r_2 r_1 & r_2 r_2 - 1 & r_2 r_3 \\ r_3 r_1 & r_3 r_2 & r_3 r_3 - 1 \end{bmatrix} \quad (1.19)$$

1.2.4 Principal states of polarization (PSP)

A principal state of polarization is an output polarization state that does not vary to first order with wavelength for a fixed input polarization state $|s\rangle$. Differentiating equation (1.5) with respect to the angular frequency ω , the PSP states are determined by solving

$$\frac{\partial}{\partial \omega} |v(\omega)\rangle_{\omega_0} = \left(\frac{\partial}{\partial \omega} U \right) |s\rangle_{\omega_0} = -i\delta |v\rangle_{\omega_0} \quad (1.20)$$

or

$$\frac{\partial}{\partial \omega} e^{-i\varphi(\omega)\omega_0} |v\rangle = -i \left(\frac{\partial}{\partial \omega} \varphi(\omega) \right) e^{-i\varphi(\omega)\omega_0} |v\rangle$$

Here δ corresponds to the propagation group delay defined as the phase differentiation with respect to frequency. From the previous equation

$$U'U^{-1} |v\rangle_{\omega_0} = -i\delta |v\rangle_{\omega_0} \quad (1.21)$$

The prime stands for the differentiation with respect to the frequency ω . Since $U'U$ is anti-Hermitian and unitary,

$$\det(U'U^{-1}) = \det(U') = \frac{\tau^2}{4} = |a'|^2 + |b'|^2 \quad (1.22)$$

hence

$$\tau = \det(U') = 2\sqrt{|a'|^2 + |b'|^2} \quad (1.23)$$

The eigenvectors of the $U'U^{-1}$ matrix are therefore the Principle States of Polarization (PSPs). For the slow PSP (noted as $|p_+\rangle$ in the Jones space and \mathbf{p}_+ in the Stokes space), δ equals $+\tau/2$; while for the fast PSP (noted as $|p_-\rangle$ in the Jones space and \mathbf{p}_- in the Stokes space) δ equals $-\tau/2$. The

quantity τ is termed the Differential Group Delay (DGD), which is the time delay between the fast and slow propagating PSP modes at the system's output. Practically, this discussion is only valid for very small frequency variations, as we were only interested in the frequency variations to the first order.

Representing an arbitrary SOP as

$$|v(\omega_0)\rangle = c_1|p\rangle + c_2|p_-\rangle \quad (1.24)$$

where c_1 and c_2 are arbitrary constants. Equation (1.24) yields for a linearly frequency-dependent output polarization

$$|v(\omega_0 + \Delta\omega)\rangle = c_1|p\rangle e^{-i\frac{\tau\Delta\omega}{2}} + c_2|p_-\rangle e^{+i\frac{\tau\Delta\omega}{2}} \quad (1.25)$$

Equation (1.25) can be represented on the Poincaré as a rotation around the slow PSP vector by an angle $\tau\Delta\omega$ (Figure 1.3).

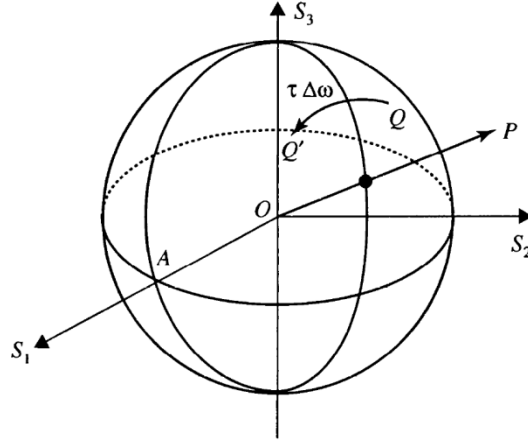


Figure 1.3 Polarization transformation on the Poincaré sphere. Q and Q' are the output SOPs at ω_0 and $\omega_0 + \Delta\omega$, respectively, for the same input SOP. $\tau\Delta\omega$ represents the rotation angle γ around the slow PSP. [2].

1.2.5 PMD vector and DGD

The Polarization Mode Dispersion (PMD) vector is defined as a vector parallel to the slow PSP and whose magnitude is the Differential Group Delay (DGD).

$$\boldsymbol{\tau} = \tau\mathbf{p} = \tau\langle p|\boldsymbol{\sigma}|p\rangle \quad (1.26)$$

Here \mathbf{p} has the direction of the slow PSP unit vector.

$$\mathbf{p} = \begin{bmatrix} p_1 \\ p_2 \\ p_3 \end{bmatrix} \quad (1.27)$$

1.2.6 Differential rotations

There are two types of infinitesimal rotations, one due to a differential birefringent system and the other type due to differential frequency changes. For a birefringent material with infinitesimal thickness dz , the output State Of Polarization (SOP) is rotated around the rotation axis, relatively to the input SOP, by an angle

$$\gamma = \delta\beta dz \quad (1.28)$$

where the birefringence $\delta\beta$ equals

$$\delta\beta = k_0\Delta n = k_0(n_{slow} - n_{fast}) \quad (1.29)$$

where n_{slow} and n_{fast} are the refractive indices of the medium along the two birefringence axes.

Similarly, a pulse with a small bandwidth - starting at ω_1 and ending at ω_2 - and a constant input SOP, experiences a rotation around PMD axis, between the output SOPs at ω_1 and ω_2 , by an angle equal to

$$\gamma = \tau\Delta\omega \quad (1.30)$$

In this case, the rotation is occurring around the PMD vector, which has the same direction as the slow PSP (Figure 1.3). That is, $R_{d\omega}$ represents the Rotation matrix that relates the output polarization at two infinitesimally separated wavelengths λ_0 and $\lambda_0 + \Delta\lambda$. The subscript $d\omega$ indicates that the rotation is with respect to the output polarizations at different wavelengths.

$$\mathbf{v}(\omega_2) = R_{d\omega} \mathbf{v}(\omega_1) \quad (1.31)$$

We can easily deduce $R_{d\omega}$ using equation(1.7) as follows

$$\begin{aligned} \because \mathbf{v}(\omega_1) &= R(\omega_1)\mathbf{s} \quad \& \quad \because \mathbf{v}(\omega_2) = R(\omega_2)\mathbf{s} \\ \therefore \mathbf{v}(\omega_2) &= R(\omega_2) R^T(\omega_1) \mathbf{v}(\omega_1) \end{aligned} \quad (1.32)$$

while from Figure 1.3 and equations (1.24) and (1.25), in the same manner as in the derivation of equation (1.19), we find

$$R_{d\omega} = \begin{bmatrix} p_1p_1 & p_1p_3 & p_1p_3 \\ p_2p_1 & p_2p_2 & p_2p_3 \\ p_3p_1 & p_3p_2 & p_3p_3 \end{bmatrix} + \sin(\tau d\omega) \begin{bmatrix} 0 & -p_3 & p_2 \\ p_3 & 0 & -p_1 \\ -p_2 & p_1 & 0 \end{bmatrix} - \cos(\tau d\omega) \begin{bmatrix} p_1p_1 - 1 & p_1p_2 & p_1p_3 \\ p_2p_1 & p_2p_2 - 1 & p_2p_3 \\ p_3p_1 & p_3p_2 & p_3p_3 - 1 \end{bmatrix} \quad (1.33)$$

And for infinitesimal changes in frequency equation (1.33) simplifies to

$$R_\omega = I + \tau d\omega \begin{bmatrix} 0 & -p_3 & p_2 \\ p_3 & 0 & -p_1 \\ -p_2 & p_1 & 0 \end{bmatrix} = I + \tau d\omega \mathbf{p} \times \quad (1.34)$$

1.3 Long fiber cable analysis, concatenated sections model [2]

To analyze the varying changes of the fiber parameters along the length of a long fiber sample, the fiber is divided into small concatenated sections.

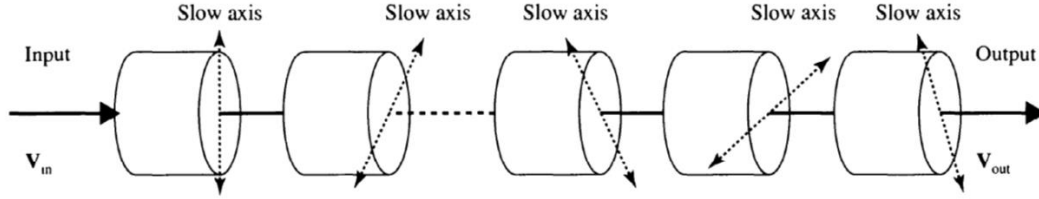


Figure 1.4 A long segment of fiber is represented by a series of birefringent elements. The slow axis of adjacent birefringent elements is arbitrary orientated. [2]

1.4 Resultant PMD vector of concatenated sections [2]

To calculate the PMD vector of a series of concatenated sections, consider first a single birefringent section as shown in Figure 1.5. Where R is the rotation matrix of the section, \mathbf{s} is the input polarization Stokes vector, \mathbf{v} is the output polarization Stokes vector and $\boldsymbol{\tau}$ is the PMD vector of the section.

$$\mathbf{v} = R \mathbf{s} \quad (1.35)$$

For infinitesimal frequency changes we have

$$\begin{aligned} \frac{\partial \mathbf{v}}{\partial \omega} &= \boldsymbol{\tau} \times \mathbf{v} = \boldsymbol{\tau} \times R \mathbf{s} = \frac{\partial R}{\partial \omega} \mathbf{s} \\ \therefore \frac{\partial R}{\partial \omega} &= \boldsymbol{\tau} \times R \Rightarrow \boldsymbol{\tau} \times = \frac{\partial R}{\partial \omega} R^{-1} \end{aligned} \quad (1.36)$$

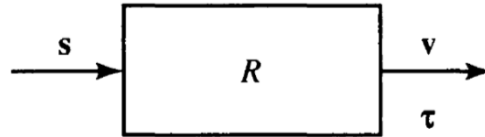


Figure 1.5 Linear input output relationship of a birefringent fiber system. [2]

For 2 successive sections with PMD vectors $\boldsymbol{\tau}_1$ and $\boldsymbol{\tau}_2$, and rotation matrices R_1 and R_2 (Figure 1.6), the resultant rotation matrix and PMD vector of the system R and $\boldsymbol{\tau}$ are then given by

$$\mathbf{v} = R_2 R_1 \mathbf{s} = R \mathbf{s} \quad (1.37)$$

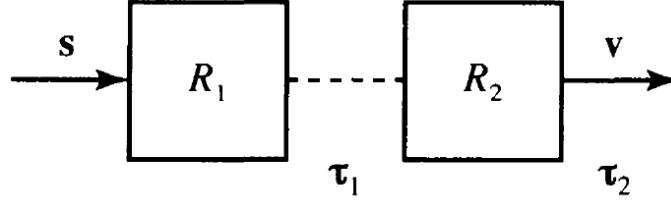


Figure 1.6 Concatenation of two birefringent sections. [2]

From equations (1.36) and (1.37)

$$\begin{aligned} \boldsymbol{\tau} \times &= \frac{\partial R}{\partial \omega} R^{-1} = \frac{\partial (R_2 R_1)}{\partial \omega} (R_2 R_1)^{-1} = \frac{\partial (R_2)}{\partial \omega} R_1 R_1^{-1} R_2^{-1} + R_2 \frac{\partial (R_1)}{\partial \omega} R_1^{-1} R_2^{-1} \\ \boldsymbol{\tau} \times &= \frac{\partial (R_2)}{\partial \omega} R_2^{-1} + R_2 \boldsymbol{\tau}_1 \times R_2^{-1} = \boldsymbol{\tau}_2 \times + R_2 \boldsymbol{\tau}_1 \times R_2^{-1} \end{aligned} \quad (1.38)$$

But $R_2 \boldsymbol{\tau}_1 \times R_2^{-1} = (R_2 \boldsymbol{\tau}_1) \times$ [2]

$$\boldsymbol{\tau} \times = \boldsymbol{\tau}_2 \times + (R_2 \boldsymbol{\tau}_1) \times \quad (1.39)$$

Hence

$$\boldsymbol{\tau} = \boldsymbol{\tau}_2 + R_2 \boldsymbol{\tau}_1 \quad (1.40)$$

Equation (1.40) is the elementary rule of a series of concatenated sections of a fiber cable.

Alternatively, in the Jones matrix formulation, to calculate the total DGD for a system of concatenated birefringent sections, a single birefringent section is considered and reference axis (x and y), the fast and slow mode axis and the angle Ψ between the two axis systems are defined as shown in Figure 1.7.

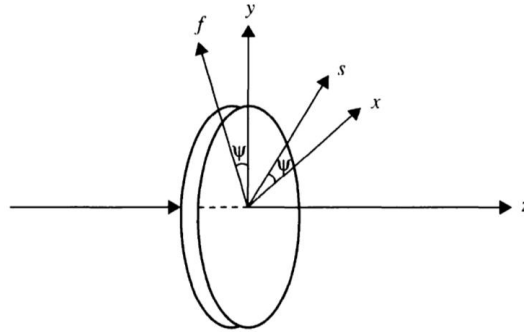


Figure 1.7 A diagram showing a birefringent section and the reference x and y axis, the fast and slow mode axis and the angle Ψ between them. [2]

The input SOP is

$$\mathbf{V} = \begin{bmatrix} V_x \\ V_y \end{bmatrix} \quad (1.41)$$

Before applying the birefringent effect, the incident SOP is decomposed into a linear combination of the fast and slow modes.

$$\begin{bmatrix} V_s \\ V_f \end{bmatrix} = \begin{bmatrix} \cos(\psi) & \sin(\psi) \\ -\sin(\psi) & \cos(\psi) \end{bmatrix} \begin{bmatrix} V_x \\ V_y \end{bmatrix} = R(\Psi) \begin{bmatrix} V_x \\ V_y \end{bmatrix} \quad (1.42)$$

Where $R(\Psi)$ is the coordinate rotation matrix and Ψ is the azimuth angle between the x-y coordinates and the slow-fast axis. Applying the birefringent effect to the decomposed input SOP,

$$\begin{bmatrix} V'_s \\ V'_f \end{bmatrix} = \begin{bmatrix} e^{-i\frac{\delta\beta}{2}d} & 0 \\ 0 & e^{+i\frac{\delta\beta}{2}d} \end{bmatrix} \begin{bmatrix} V_s \\ V_f \end{bmatrix} = W \begin{bmatrix} V_s \\ V_f \end{bmatrix} \quad (1.43)$$

in which

$$\delta\beta = \beta_s - \beta_f \quad (1.44)$$

and d is the thickness of the birefringent section. To express the output SOP with respect to the x-y coordinates, the output is multiplied by $R(-\Psi)$

$$\begin{bmatrix} V'_x \\ V'_y \end{bmatrix} = \begin{bmatrix} \cos(\psi) & -\sin(\psi) \\ \sin(\psi) & \cos(\psi) \end{bmatrix} \begin{bmatrix} V'_s \\ V'_f \end{bmatrix} = R(-\Psi) \begin{bmatrix} V'_s \\ V'_f \end{bmatrix} \quad (1.45)$$

Summing the previous mathematical discussion,

$$\begin{aligned} \begin{bmatrix} V'_x \\ V'_y \end{bmatrix} &= \begin{bmatrix} \cos(\psi) & \sin(\psi) \\ -\sin(\psi) & \cos(\psi) \end{bmatrix} \begin{bmatrix} e^{-i\frac{\delta\beta}{2}d} & 0 \\ 0 & e^{+i\frac{\delta\beta}{2}d} \end{bmatrix} \begin{bmatrix} \cos(\psi) & -\sin(\psi) \\ \sin(\psi) & \cos(\psi) \end{bmatrix} \begin{bmatrix} V_x \\ V_y \end{bmatrix} \\ &= R(-\Psi)WR(-\Psi) \begin{bmatrix} V_x \\ V_y \end{bmatrix} \end{aligned} \quad (1.46)$$

Note that in this discussion the propagation phase φ was not included, where

$$\varphi = \frac{1}{2}(n_s + n_f) \frac{2\pi}{\lambda} d \quad (1.47)$$

In order to calculate the total effect of the birefringence of all the sections, equation (1.46) is expressed in its recursive form

$$\begin{bmatrix} V'_x \\ V'_y \end{bmatrix}_n = R(-\Psi_n) W_n R(-\Psi_n) \begin{bmatrix} V'_x \\ V'_y \end{bmatrix}_{n-1} \quad (1.48)$$

in which the subscript n represents the section number and the input SOP is represented as $\begin{bmatrix} V'_x \\ V'_y \end{bmatrix}_0$.

1.5 Measuring DGD in lab environment

Our measurement of the DGD requires the determination of the 3×3 matrix $R_{d\omega}$. The method employed as described in [4] requires determining 2 matrices as follows,

$$\begin{bmatrix} s_1^{p_1} & s_1^{p_2} & s_1^{p_3} \\ s_2^{p_1} & s_2^{p_2} & s_2^{p_3} \\ s_3^{p_1} & s_3^{p_2} & s_3^{p_3} \end{bmatrix}_{\lambda_2} = R_{d\omega} \begin{bmatrix} s_1^{p_1} & s_1^{p_2} & s_1^{p_3} \\ s_2^{p_1} & s_2^{p_2} & s_2^{p_3} \\ s_3^{p_1} & s_3^{p_2} & s_3^{p_3} \end{bmatrix}_{\lambda_1} \quad (1.49)$$

$$Q' = R_{d\omega} Q$$

This is accomplished by measuring three output polarizations at two slightly different wavelengths. Here Q' and Q represent the output at λ_2 and λ_1 respectively, while superscripts p_1 , p_2 and p_3 refer to differing input polarizations. Thus $s_1^{p_1}$ is the first Stokes parameter of the output polarization when the input polarization is p_1 . More than three polarizations can be used to calculate R to give a better accuracy while calculating $R_{d\omega}$. In this case, the above equation is rearranged as

$$Q'^T = Q^T R_{d\omega}^T \quad (1.50)$$

which is in the form of the Orthogonal Procrustes problem [5] which solves

$$AT = B + E \quad (1.51)$$

where A and B are known matrices, and T is the matrix relating A and B such as E , the residual matrix, is minimal. T is obtained from the singular value decomposition of

$$M = U \Sigma V^T \quad (1.52)$$

where

$$M = A^T B \quad (1.53)$$

and hence

$$T = U V^T \quad (1.54)$$

For an M matrix of dimensions $m \times n$ the dimensions of U is $m \times m$, Σ is $m \times n$ and V^T is $n \times n$. Hence T possesses the same dimensions as M . Accordingly writing

$$R_{d\omega}^T = U V^T \Rightarrow R_{d\omega} = V U^T \quad (1.55)$$

To calculate τ from R we use equation (1.33) instead of equation (1.34) with the following technique for improved accuracy

$$dR_{d\omega} = \frac{(R_{d\omega} - R_{d\omega}^T)}{2} = \sin(\tau d\omega) \begin{bmatrix} 0 & -p_3 & p_2 \\ p_3 & 0 & -p_1 \\ -p_2 & p_1 & 0 \end{bmatrix} \quad (1.56)$$

As $dR_{d\omega}$ is a 3×3 matrix with zero diagonal elements, the third element of the 2nd column is equal $p_1 \sin(\tau d\omega)$, while the first element of the 3rd column equals $p_2 \sin(\tau d\omega)$ and the second element of the 1st column is $p_3 \sin(\tau d\omega)$. These components define a vector whose direction is the slow PSP vector with magnitude $\sin(\tau d\omega)$. Subsequently $\cos(\tau d\omega)$ is given from equation (1.33) according to

$$\cos(\tau d\omega) = \frac{\text{Trace}(R_{d\omega}) - 1}{2} \quad (1.57)$$

From $\sin(\tau d\omega)$ and $\cos(\tau d\omega)$ the angle of rotation $\tau d\omega$ and hence τ are determined for a given $d\omega$.

Chapter 2

Relaxation of stress and strain in fibers

In this chapter we examine the stresses that induce birefringence in an optical fiber and how these stresses relax with time by following the analysis presented by G.W. Scherer [6]. Although the formulation of [6] is developed for stresses in glass at high temperatures (> 200 to 100°C) for manufacturing and annealing processes, we present some of the basic formulas of great importance to understand the latter part of the thesis.

2.1 Overview

By definition the uniaxial strain ε_i is related to the applied stress σ_i on a body as follows

$$\varepsilon_1 = \frac{\sigma_1}{E}, \quad \varepsilon_2 = \frac{\sigma_2}{E}, \quad \varepsilon_3 = \frac{\sigma_3}{E} \quad (2.1)$$

in Cartesian space where E is the Young modulus of the material (see Figure 1 Figure 2.1); where the i subscript represents the stress and strain direction assuming that it acts perpendicularly on the body's surface. Applying the above stress to a cube alters its dimensions from L_0 to

$$L_1 = L_0(1 + \varepsilon_1), \quad L_2 = L_0(1 + \varepsilon_2), \quad L_3 = L_0(1 + \varepsilon_3) \quad (2.2)$$

yielding a volume, after neglecting all second-order terms,

$$V = L_1 L_2 L_3 = L_0^3 (1 + \varepsilon_1 + \varepsilon_2 + \varepsilon_3) \quad (2.3)$$

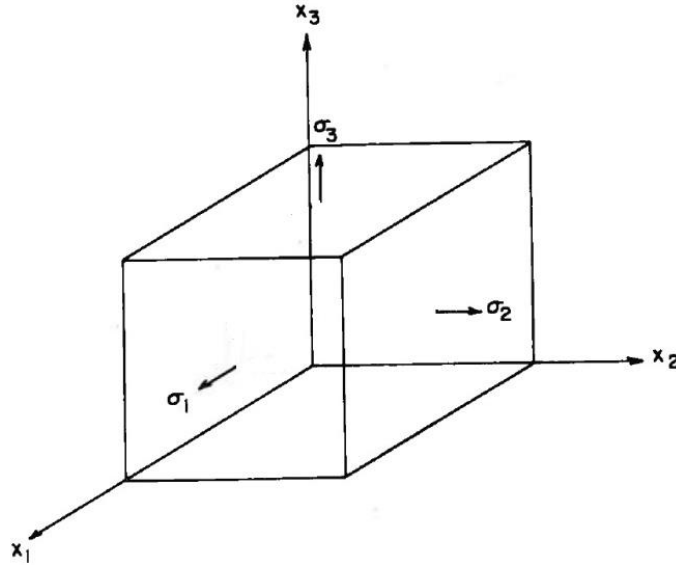


Figure 2.1 Coordinate system and components of stress [6].

thus

$$\frac{V - L_0^3}{L_0^3} = \frac{\Delta V}{V} = \varepsilon_1 + \varepsilon_2 + \varepsilon_3 = \varepsilon \quad (2.4)$$

For solely uniaxial stresses applied on Figure 2.1's body

$$\frac{\Delta V}{V} = (1 - 2N)\varepsilon_1 \quad (2.5)$$

where N is the Poisson's ratio of the cube's material. The constitutive equations relate stresses and strains in an isotropic material according to

$$\begin{aligned} \varepsilon_1 &= \varepsilon_f + \frac{1}{E} [\sigma_1 - N(\sigma_2 + \sigma_3)] \\ \varepsilon_2 &= \varepsilon_f + \frac{1}{E} [\sigma_2 - N(\sigma_1 + \sigma_3)] \\ \varepsilon_3 &= \varepsilon_f + \frac{1}{E} [\sigma_3 - N(\sigma_1 + \sigma_2)] \end{aligned} \quad (2.6)$$

where ε_f is the free strain caused by thermal expansion ($\varepsilon_f = \alpha\Delta T$ where α is the linear thermal expansion coefficient). The pure dilatation (volume changing or hydrostatic [6]) stress and strain are

$$\varepsilon = \varepsilon_1 + \varepsilon_2 + \varepsilon_3 \quad (2.7)$$

and

$$\sigma = \sigma_1 + \sigma_2 + \sigma_3 \quad (2.8)$$

Because ε is the relative volume change and σ is the dilatational stress, then

$$\sigma = 3K\varepsilon \quad (2.9)$$

where K is the bulk modulus. The following relation can be easily derived

$$K = \frac{E}{3(1 - 2N)} \quad (2.10)$$

For $N=1/2$, K is infinite indicating that the material is incompressible.

2.2 Viscoelasticity of glass

The viscoelastic property of glass allows it to react instantaneously to stresses with an elastic behavior and in the same time react with a delayed strain without a true viscous flow. This can be modeled with a spring in series with a Voigt element (see Figure 2.2). A Voigt element consists of a spring and a dash pot (filled with a viscous fluid) connected in parallel. The strain in both the Voigt's element spring and the dash pot are equal but the stress on each is different. The stress across the model in Figure 2.2 is constant, but the strain in the spring K_1 and the Voigt element are not equal.

This model assumes pure dilatational strain (i.e. no shear stresses and hence no deformation of the substance)

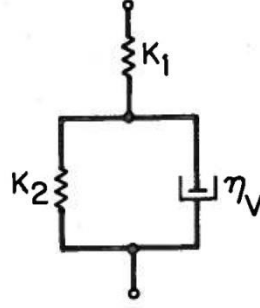


Figure 2.2 A Voigt element in series with a spring to model the viscoelasticity of glass [6].

According to Scherer [6] the instantaneous elastic strain ε^E

$$\varepsilon^E(t) = \frac{\sigma(t)}{3K_1} \quad (2.11)$$

and the Voigt element follows the following relation

$$\sigma(t) = 3K_2\varepsilon^D(t) + \eta_V\dot{\varepsilon}^D(t) \quad (2.12)$$

where η_V is the volume viscosity of glass, ε^D is the delayed strain and $\dot{\varepsilon}^D$ is the time derivative of the delayed strain. The solution of the previous equation is [6]

$$\varepsilon^D(t) = \int_0^t \frac{\sigma(t')}{\eta_V} e^{-(t-t')/\tau_D} dt' \quad (2.13)$$

where τ_D is the dilatational retardation time

$$\tau_D = \frac{\eta_V}{3K_2} \quad (2.14)$$

Then the total strain is

$$\varepsilon_{total} = \varepsilon_f + \varepsilon^E + \varepsilon^D \quad (2.15)$$

The following relation between K_1 and K_2 can be deduced if constant stress is assumed in (2.13) when $t \rightarrow \infty$ [6].

$$\frac{1}{K} = \frac{1}{K_1} + \frac{1}{K_2} \quad (2.16)$$

2.3 Mechanical constants of glass

Glass can be doped with different elements at different concentrations to alter its mechanical and / or optical properties. Although the mechanical properties of glass proved to affect its optical parameters (ex: birefringence), they are not discussed in depth.

2.3.1 Young's Modulus of glass

References [7] and [8] suggest different Young's modulus values (Figure 2.3 and Figure 2.4). The value of Young's modulus that best suited our model (to be discussed in Chapter 5) was found to be around 68 Giga Pascal. This value lies in the reasonable range mentioned by Morey [7] and Philips [8].

TABLE XII. 3. ELASTIC CONSTANTS OF SILICA GLASS*

Bulk modulus	K	370	kilobars
Rigidity modulus	R	305	kilobars
Young's modulus	E	700	kilobars
Poisson's ratio	σ	0.14	kilobar

* Unit: 1 kilobar = 10^8 bars = 10^9 dynes per sq. cm.
 1 bar = 1.020 Kg./cm.² = 14.50 lb./in.²

Figure 2.3 Some mechanical constants of silica glass [7].

TABLE 4.1--Properties of Some Multi-component Glasses

Number (Table 3.7)	Type (Table 3.7)	Density (g. per cu. cm.)	Young's Modulus (kg. per sq. mm.)	Poisson's Ratio (dimensionless)	Thermal Expansion $\left(\frac{10^6 \Delta l}{l \Delta t}\right)$ (Range indicated—°C.)	Specific Heat (g.-cal. per g.)
1	496/644	2.370 ^a	7300	0.197 ^a	0.204 ^a
4	511/640	2.47 ^a	7470	0.210 ^a
6	513/637	2.47 ^a	7970	0.213 ^a	79.7(17.5-94.7) ^a
7	513/573	2.572 ^a	6500	0.226 ^a
11	517/602	2.580 ^a	6600	0.231 ^a	96.3(17-95.5) ^a
27	573/576	3.21 ^a	7420	0.252 ^a	79.0(18.9-93.1) ^a
34	610/574	3.532 ^a	8000	0.271 ^a	0.140 ^a
40	645/341	3.879 ^a	5460	0.224 ^a
43	751/276	4.731 ^a	5480	0.239 ^a
46	905/217	5.944 ^a	5080	0.261 ^a	93.3(24.5-84) ^a
55	165 ^{III}	2.479 ^a	7320	0.196 ^a
59		2.629 ^a	6650
61	Thermometer,	2.585 ^a	7470	0.228 ^a	80.3(14.6-92.2) ^a
64	16 ^{III}	2.518 ^a	6000	0.253 ^a	0.189 ^a
66		2.668 ^a	5850	0.261 ^a
68		3.578 ^a	5380
48	507/614	2.243 ^a	4710	0.274 ^a	67.1(14.4-94.4) ^a	0.218 ^a
52	653/508	3.527 ^a	8170	0.319 ^a	33.3(10.4-92.9) ^a	0.166 ^a
71	522/697	2.588 ^a	6770	0.235 ^a
72	558/670	3.070 ^a	6330	0.253 ^a	87.0(20.3-92.2) ^a	0.159 ^a
	Pyrex chem.-resistant	2.23	6230	33.0(19-350) ^a	0.20

^a A. Winkelmann and O. Schott, *Ann. Physik Chem.*, 51, 697 (1894).
^b A. Winkelmann, *Ann. Physik Chem.*, 49, 401 (1893).
^c E. Zschimmer, in C. Doelter, *Handbuch der Mineralchemie*, 1, 869, Dresden and Leipzig, 1912.

^d R. Straubel, *Ann. Physik Chem.*, 68, 369 (1899).
^e C. Pulfrich, *Ann. Physik Chem.*, 45, 609 (1892).
^f H. Hovestadt, *Jena Glass*, The Macmillan Co., New York, 1902.

Figure 2.4 Mechanical constants of different types of glass [8].

2.3.2 Viscosity and Volume Viscosity

The Viscosity of glass is usually studied around melting and annealing temperatures. Therefore we will use the curves in [6] to find the different values of viscosity at room temperature by extrapolation. Doing so we find that the viscosity of different types of glass, suggested by Mazurin et al. ([6] pages 148-151) (Figure 2.5), varies between 10^{17} and 10^{25} (Pascal.second). On the other hand Zijlstra's measurements (Figure 2.6, [6] page 148-151) suggest that the viscosity of glass changes slope after 400° . Extrapolating Zijlstra's measurements would result a viscosity varying between $10^{18.5}$ and 10^{17} (Pascal.Second).

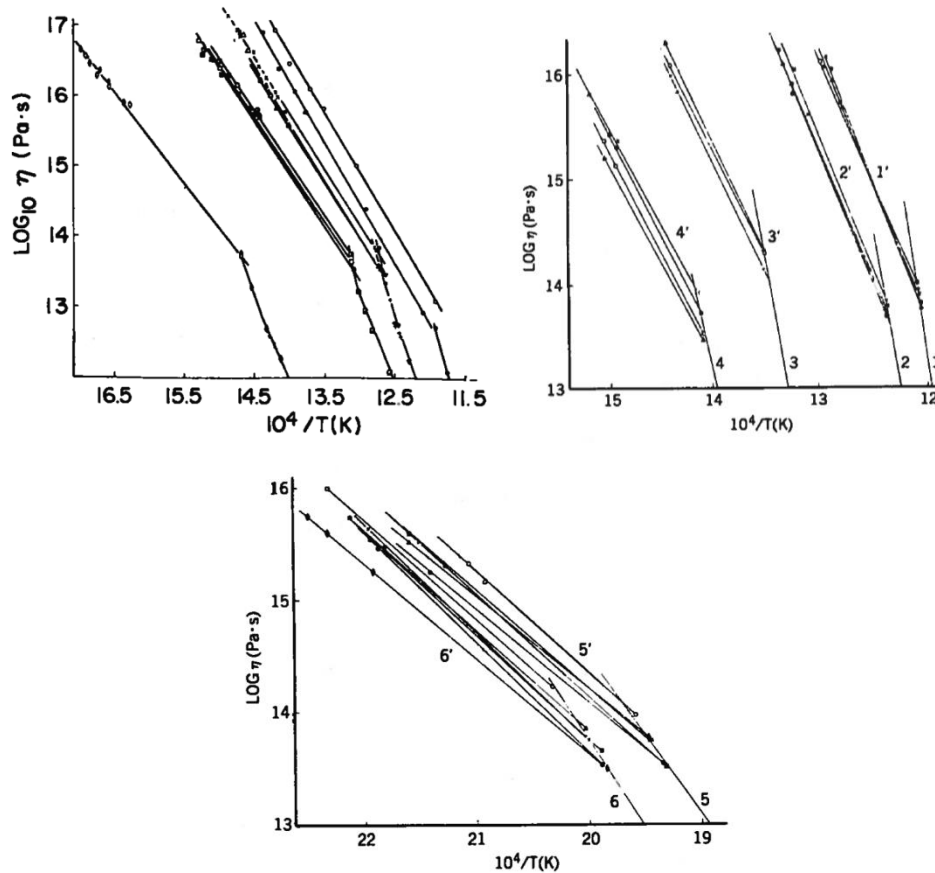


Figure 2.5 Mazurin et al. - viscosity measurements versus temperature for different types of glass [6] (pages 149-150).

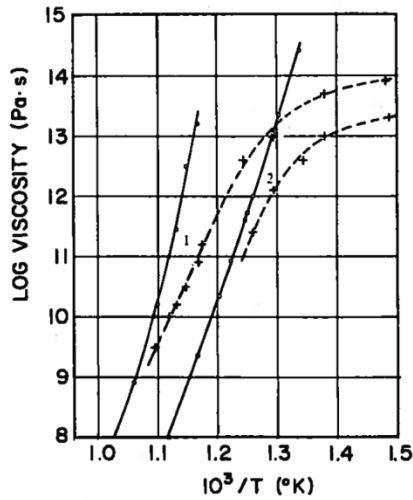


Figure 2.6 Zijlstra's - viscosity measurements versus temperature for different types of glass [6] (pages 149-151).

According to J. Lyklema and H. Van Olphen [9], the *Shear Viscosity*, also known as simply *Viscosity*, is defined as the constant relating shear stress and rate of strain at a point in the fluid; while the *Volume viscosity*, also known as *Bulk Viscosity* or *Dilatational Viscosity*, describes the flow of fluids whenever a change of volume due to the flow is present.

Although the property we are interested in is the volume viscosity, and because measurements of volume viscosity of glass are unavailable, it seems reasonable to assume that the value of volume viscosity should be comparable to shear viscosity. Therefore we assumed 5×10^{20} (Pascal.Second) which best fit our simulations Chapter 5 and which was also close to range of measurements of the shear viscosity.

2.4 Optical properties of glass

2.4.1 Refractive index and temperature [10]

J. Wary and J. Neu measured the refractive index changes of fused silica with temperature at different wavelengths for the purpose of characterizing optical equipment in the upper atmosphere where it is vulnerable to very large temperature variations. According to the following tables they found that the rate of change of the refractive index is in the order of 7.9×10^{-6} to 19.6×10^{-6} /°Celsius.

Table 2-1 "Refractive index vs temperature, fused silica, Corning code 7940, ultraviolet grade" [10]

λ Microns	n 26°C	n 471°C	$(dn/dT)/$ °C×10 ⁶	n 828°C	$(dn/dT)/$ °C×10 ⁶
0.23021	1.52034	1.52908	+19.6	1.53584	+19.3
0.23783	1.51496	1.52332	+18.8	1.52985	+18.6
0.2407	1.51361	1.52201	+18.9	1.52832	+18.3
0.2465	1.50970	1.51774	+18.1	1.52391	+17.7
0.24827	1.50865	1.51665	+18.0	1.52289	+17.8
0.26520	1.50023	1.50763	+16.6	1.51351	+16.5
0.27528	1.49615	1.50327	+16.0	1.50899	+16.0
0.28035	1.49425	1.50143	+16.2	1.50691	+15.8
0.28936	1.49121	1.49818	+15.7	1.50358	+15.4
0.29673	1.48892	1.49584	+15.6	1.50112	+15.2
0.30215	1.48738	1.49407	+15.1	1.49942	+15.0
0.3130	1.48462	1.49126	+14.9	1.49641	+14.7
0.33415	1.48000	1.48633	+14.2	1.49135	+14.1
0.36502	1.47469	1.48089	+14.0	1.48563	+13.6
0.40466	1.46978	1.47575	+13.4	1.48033	+13.2
0.43584	1.46685	1.47248	+12.7	1.47716	+12.9
0.54607	1.46028	1.46575	+12.3	1.47004	+12.2
0.5780	1.45899	1.46429	+11.9	1.46870	+12.1
1.01398	1.45039	1.45562	+11.8	1.45960	+11.5
1.12866	1.44903	1.45426	+11.8	1.45820	+11.4
1.254 ^a	1.44772	1.45283	+11.5	1.45700	+11.6
1.36728	1.44635	1.45140	+11.4	1.45549	+11.4
1.470 ^a	1.44524	1.45031	+11.4	1.45440	+11.4
1.52952	1.44444	1.44961	+11.6	1.45352	+11.3
1.660 ^a	1.44307	1.44799	+11.1	1.45174	+10.8
1.701	1.44230	1.44733	+11.3	1.45140	+11.3
1.981 ^a	1.43863	1.44361	+11.2	1.44734	+10.9
2.262 ^a	1.43430	1.43933	+11.3	1.44306	+10.9
2.553 ^a	1.42949	1.43450	+11.3	1.43854	+11.3
3.00 ^a	1.41995	1.42495	+11.2	1.42877	+11.0
3.245 ^a	1.41353	1.41893	+12.2	1.42243	+11.1
3.37 ^a	1.40990	1.41501	+11.5	1.41915	+11.5

^a Wavelength determination by narrow-bandwidth interference filters.

Table 2-2 "Refractive index vs temperature, alumino-silicate glass, Corning code 1723" [10]

λ Microns	n 28°C	n 526°C	$(dn/dT)/$ °C×10 ⁶
0.36502	1.57093	1.57645	+11.1
0.40466	1.56405	1.56914	+10.2
0.43584	1.56000	1.56487	+9.8
0.54607	1.55100	1.55548	+9.0
0.5780	1.54928	1.55366	+8.8
1.01398	1.53854	1.54260	+8.2
1.12866	1.53699	1.54101	+8.1
1.36728	1.53419	1.53814	+7.9
1.470 ^a	1.53292	1.53687	+7.9
1.52952	1.53224	1.53619	+7.9
1.660 ^a	1.53078	1.53476	+8.0
1.701	1.53014	1.53408	+7.9
1.981 ^a	1.52648	1.53044	+8.0
2.262 ^a	1.52245	1.52643	+8.0
2.553 ^a	1.51778	1.52181	+8.1
2.665 ^a	1.51578	1.51998	+8.4

^a Wavelength determination by narrow-bandwidth interference filters.

Table 2-3 “Refractive index vs temperature, Vycor Corning code 7913, optical grade” [10]

λ Microns	n 28°C	n 526°C	$(dn/dT)/$ °C×10 ⁶	n 826°C	$(dn/dT)/$ °C×10 ⁶
0.26520	1.49988	1.50799	+16.3	1.51438	+18.2
0.28936	1.49074	1.49831	+15.2	1.50418	+16.8
0.29673	1.48851	1.49587	+14.8	1.50164	+16.5
0.30215	1.48694	1.49423	+14.6	1.49990	+16.2
0.3130	1.48416	1.49121	+14.2	1.49679	+15.8
0.33415	1.47949	1.48622	+13.5	1.49158	+15.2
0.36502	1.47415	1.48065	+13.1	1.48570	+14.5
0.40466	1.46925	1.47547	+12.5	1.48027	+13.8
0.43584	1.46628	1.47234	+12.2	1.47708	+13.5
0.54607	1.45960	1.46544	+11.7	1.46992	+12.9
0.5780	1.45831	1.46407	+11.6	1.46849	+12.8
1.01398	1.44968	1.45526	+11.2	1.45924	+12.0
1.12866	1.44831	1.45373	+10.9	1.45779	+11.9
1.254 ^a	1.44677	1.45222	+10.9	1.45627	+11.9
1.36728	1.44554	1.45095	+10.9	1.45504	+11.9
1.470 ^a	1.44422	1.44965	+10.9	1.45370	+11.9
1.52952	1.44356	1.44896	+10.8	1.45306	+11.9
1.660 ^a	1.44206	1.44750	+11.0	1.45157	+11.9
1.701	1.44137	1.44677	+10.8	1.45088	+11.9
1.981 ^a	1.43750	1.44291	+10.9	1.44702	+11.9
2.262 ^a	1.43298	1.43839	+10.9	1.44258	+12.0
2.553 ^a	1.42825	1.43373	+11.0	1.43824	+12.5

^a Wavelength determination by narrow-bandwidth interference filters.

These values of rate of change of the refractive index with temperature give us an order of magnitude estimate while constructing our mathematical model later; as we don't know the material of the fiber based DCM under test.

Chapter 3

Previous work and literature review

Below, we overview the background literature related to our work. The first section discusses the temperature behavior of fiber based optical components while the second section discusses mathematical models that predict the influence of mechanical and temperature variations on birefringence. These provide important input to our model of a DCM and enable us later to qualitatively predict the DCM's fiber behavior.

3.1 Temperature measurements for different fiber based optical components

3.1.1 Time evolution measurements on installed fibers

This subsection summarizes previous studies of the DGD behavior of installed fibers. In [11], De Angelis et al. measured the DGD of a terrestrial fiber located in Italy. The buried cable consisted of 8 sections of fiber connected to each other. During 27 hours long measurements, over two sections of cable, the temperature dependent variation of the DGD was recorded during sunrise and sunset. The two measurements revealed similar behavior (Figure 3.1 and Figure 3.2) with pronounced DGD changes during sunrise and sunset, resulting from the large temperature fluctuations over these periods [11].

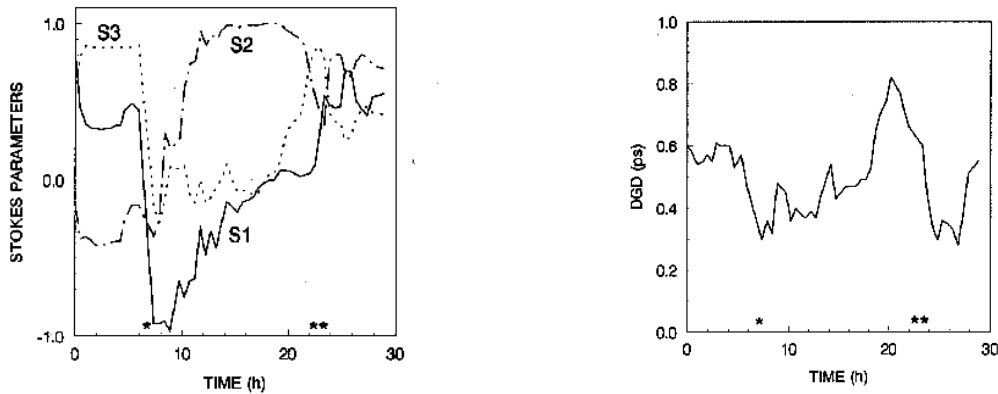


Figure 3.1 “Time evolution of the normalized stokes vector (left side graph) and that of the DGD (right side graph) of the first measurement (sunset = *, sunrise = **)” [11]

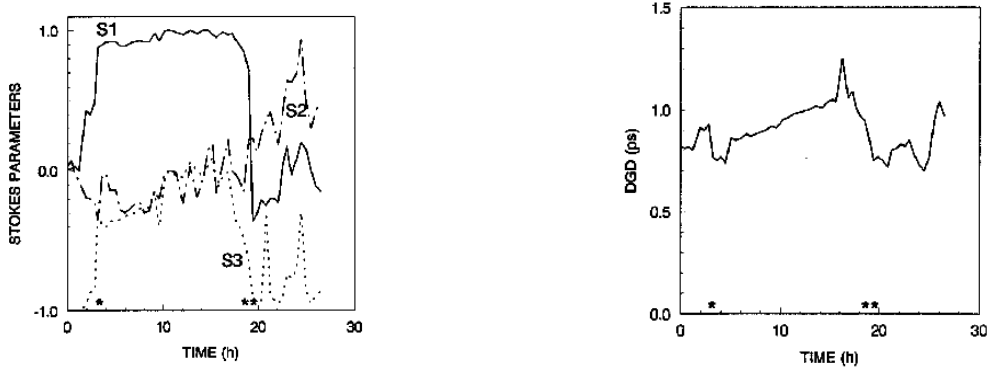


Figure 3.2 “Time evolution of the normalized stokes vector (left side graph) and that of the DGD (right side graph) of the second measurement (sunset = *, sunrise = **)” [11]

Similarly, Takahashi et al. performed a measurement on a 120 km long submarine cable with 86% of its length submerged [12]. Here the DGD changed on a time scale of few hours (4 to 5 hours) according to their data which suggested that the fluctuations resulted from daily temperature changes.

At New Brunswick University, J. Cameron et al. conducted a DGD measurement on a 36 Km single mode spool of fiber enclosed in a temperature controlled chamber; they also did a DGD measurement on a 48.8 Km buried cable and on a 96 Km areal cable [13]. The temperature was changed rapidly during the measurement (Figure 3.3). Note that, when the temperature returns to its initial value, the DGD is steady again and has a slightly different value to the initial DGD at the beginning of the experiment; similar behavior will be further discussed in Chapter 4. Cameron et al. also compared the DGD behavior of the buried and areal cables they tested (Figure 3.4). They concluded that high rates of temperature changes yields rapid DGD fluctuations and that, consequently, the DGD of buried or submarine fibers fluctuate less than that of aerial fibers, as they are less subject to temperature changes.

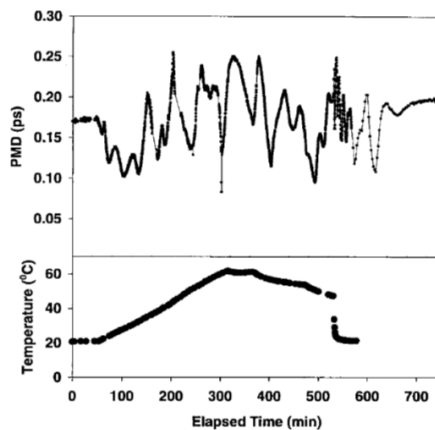


Figure 3.3 “Time evolution of PMD (upper curve), and temperature at the outside of the 36 km fiber spool (lower curve)” [13]

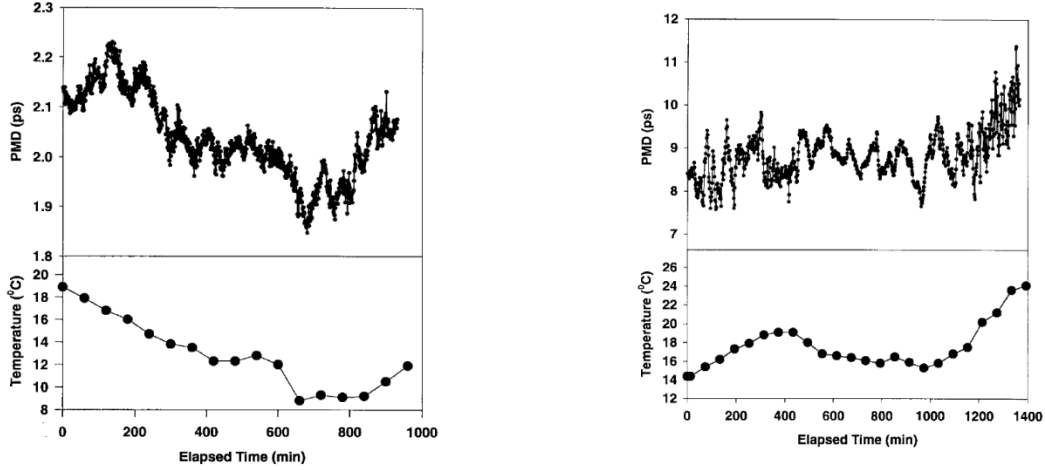


Figure 3.4 “Time evolution of PMD (upper curves), and temperature measured a meter above ground (lower curves) for the 48.8 Km buried cable (left side curves) and the 96 Km aerial cable (right side curves)” [13]

M. Brodsky et al. performed long-term DGD measurements for more than 20 days [14]. The tested cable was mainly buried but with several exposed sections, rendering it vulnerable to weather conditions. Figure 3.5 shows the difference in DGD (from the initial value) for 48 hours (left axis) and the corresponding temperature (right axis). Clearly, the DGD is highly influenced by temperature changes. A plot of the DGD temperature relation displayed a linear like relation between the DGD and temperature (Figure 3.6).

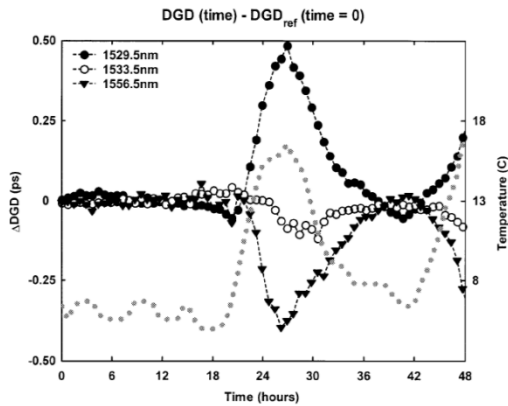


Figure 3.5 “Changes of Δ DGD for 3 wavelengths, $\lambda=1529.5 \mu\text{m}$ (\bullet), $\lambda=1533.5 \mu\text{m}$ (\circ) and $\lambda=1556.5 \mu\text{m}$ (\blacktriangledown), as a function of time (left axis). The thick dotted lines (\bullet) is the ambient temperature (right axis)” [14]

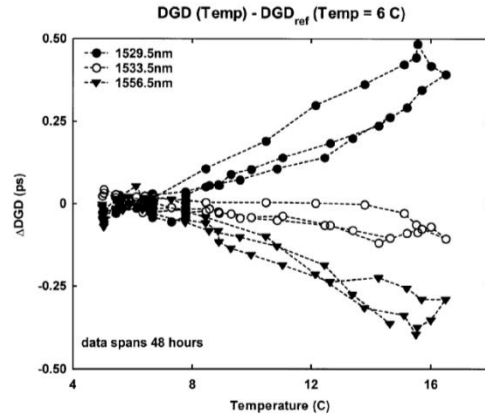


Figure 3.6 Same data as previous figure but presented as a function of temperature ($\lambda=1529.5 \mu\text{m}$ (\bullet), $\lambda=1533.5 \mu\text{m}$ (\circ) and $\lambda=1556.5 \mu\text{m}$ (\blacktriangledown)) [14]

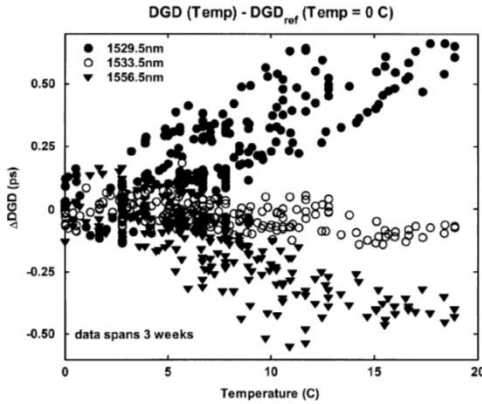


Figure 3.7 “Plot similar to Figure 3.6, but with a data span over 3 weeks of measurements” [14]

Figure 3.7 shows the difference in DGD versus temperature over a 21 days span. Although the linear like relation is still present, the data points were spread more randomly (compared to Figure 3.6) than linearly. Brodsky et al. concluded that, over long terms, the fiber cable experience irreversible variations; while over short time spans, temperature variations induce reversible DGD changes.

3.1.2 Dispersion compensation modules (DCMs) under temperature variations

T. Geisler and P. Kristensen tested DCMs under different temperatures in a controlled environment (climate chamber) [15]. In the first measurement, the temperature was varied periodically; where each period started by a temperature increase from 25°C to 35°C in two hours. The chamber’s temperature was then held at 35°C for five minutes followed by a temperature decrease to 25°C over 25 minutes period. Finally the temperature was held at 25°C for one hour. This cycle was repeated 6 times. The resulting measured DGD, for 2 different DCMs, is displayed as the grey scale diagram of Figure 3.8. It should be noted that, although the DGD is almost periodic with every temperature cycle, the DGD value is not the same –for most wavelengths– for the same temperature during the same cycle.

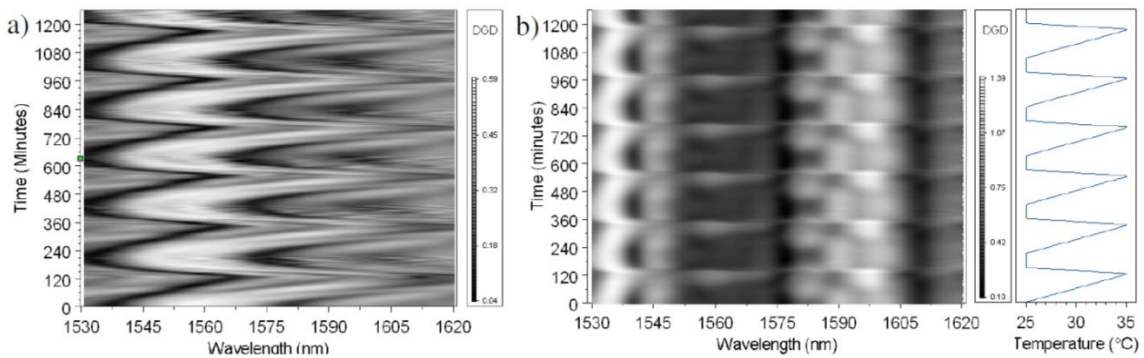


Figure 3.8 “Grey-scale plots of the DGD spectra as a function of time during 6 temperature cycles (far right side). a) DCM#1 b)DCM#2” [15]

Geisler and Kristensen also shocked DCM#2 thermally by changing the temperature from 25°C to 75°C in 20 minutes, maintaining the temperature for seven hours at 75°C and then passively cool it back to 25°C. Figure 3.9 (a) shows the grey-scale of the DGD measurement for DCM#2 during the thermal shock; while Figure 3.9 (b) shows the DGD spectra before and after the 6 temperature cycles, after the thermal shock and after 2 temperature cycles. They concluded that due to the thermal shock the DCM have experienced irreversible changes, which is not the case when the temperature was changing in a 10°C span. They also experienced DGD changes due to mechanical perturbations.

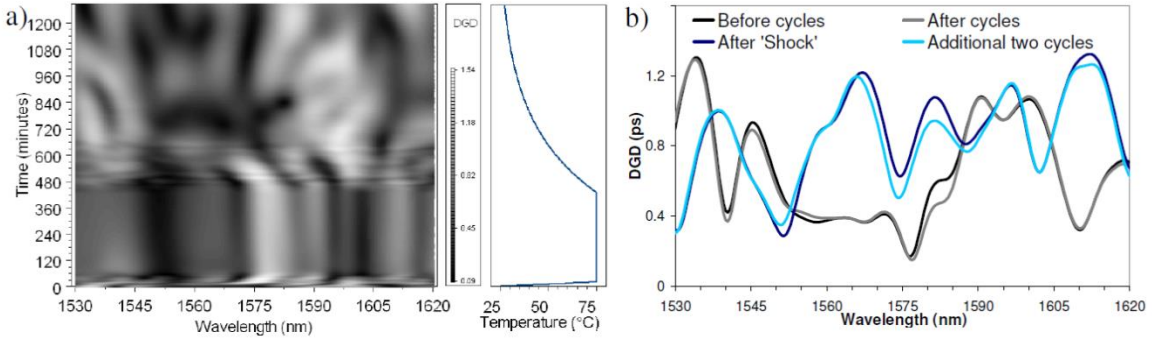


Figure 3.9 “a) Grey-scale plots of the DGD spectra as a function of time during thermal shock, with temperature profile to the right. b) DGD spectra before (black) temperature cycles and after the thermal shock (dark blue) and after two temperature cycles (light blue)” [15]

3.2 Mathematical models of mechanical and temperature effects on birefringence

As discussed earlier, the birefringence of optical fibers results from both geometrical deformation (i.e. the fiber core is not perfectly circular) and mechanical stresses. The mechanical stresses result from bending, bending under tension, twisting and by built in stresses due to non-perfect circular shape of the core and cladding. In this section we will present mathematical models for each source of birefringence.

3.2.1 Birefringence due to geometrical deformation

Although an ideal fiber possesses a perfectly circular core and cladding, a manufactured fiber deviates from cylindrical symmetry as a result of imperfections in the manufacturing process. The ellipticity e of an actual fiber is

$$e = \sqrt{1 - \frac{\rho_y}{\rho_x}} \quad (3.1)$$

where ρ_x and ρ_y are the semi-major axis and the semi-minor axis respectively (Figure 3.10). The ellipticity varies along the fiber length.

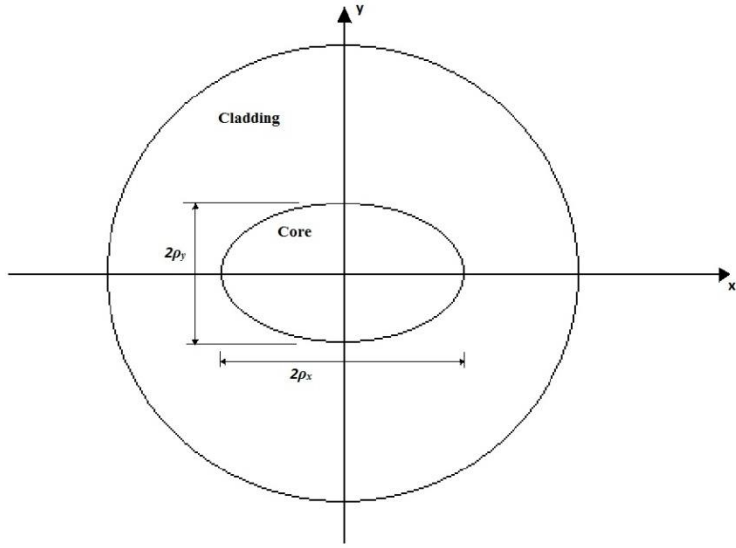


Figure 3.10 Elliptical core fiber's diagram

Many references ([16] [17] [18] [19]) discuss birefringence due to core ellipticity. J. D. Love et al. formulation is used [17].

$$\delta\beta_G = \beta_x - \beta_y = \frac{e^2(2\Delta)^3}{\rho} \frac{W^2}{8V^3} \left[U^2 + (U^2 - W^2) \left\{ \frac{J_0(U)}{J_1(U)} \right\}^2 + U W^2 \left\{ \frac{J_0(U)}{J_1(U)} \right\}^3 \right] \quad (3.2)$$

{for $\Delta \ll 1, e^2 \ll 1$ }

where $\delta\beta_G$ is the birefringence due to the geometrical form of the core, β_x and β_y are the propagating constants of the x-polarized and y-polarized fundamental modes respectively, e is the core ellipticity, Δ is the relative refractive index, ρ is the average core, V is the normalized frequency, U & W are the usual circular waveguide parameters (core and cladding parameters respectively [19]) and J is the Bessel function of the first kind.

$$\Delta = \frac{n_c^2 - n_{cl}^2}{2n_c^2} \quad (3.3)$$

$$V = \frac{2\pi}{\lambda} \rho n_c \sqrt{2\Delta} = k_0 \rho n_c \sqrt{2\Delta}$$

Where n_c and n_{cl} are the refractive indices of the core and cladding respectively and k_0 is the free space propagation constant of the wave. U and V are obtained from ([2] [19])

$$\begin{aligned}
U &= \rho \sqrt{k_0^2 n_c^2 - \beta^2} \\
W &= \rho \sqrt{\beta^2 - k_0^2 n_{cl}^2} \\
\rho(k_0^2 n_c^2 - k_0^2 n_{cl}^2) &= U^2 + W^2 \\
U \frac{J_{-1}(U)}{J_0(U)} &= -W \frac{K_{-1}(W)}{K_0(W)}
\end{aligned} \tag{3.4}$$

In which β is the propagation constant of the mode in the core and K is the modified Bessel function.

3.2.2 Birefringence due to built-in stresses [20]

During the manufacturing process, a fiber is free of stresses at the softening temperature. When it starts to cool, stresses begin to build up due to the different expansion coefficients between the core and the cladding. If the fiber was perfectly circular these stresses would not generate birefringence; however, the small ellipticity of the fiber core and the stresses lead to a polarization dependent birefringence. Eickhoff studied both cases of a fiber with a circular core and an elliptical cladding and that of fiber with an elliptical core and a circular cladding (Figure 3.11).

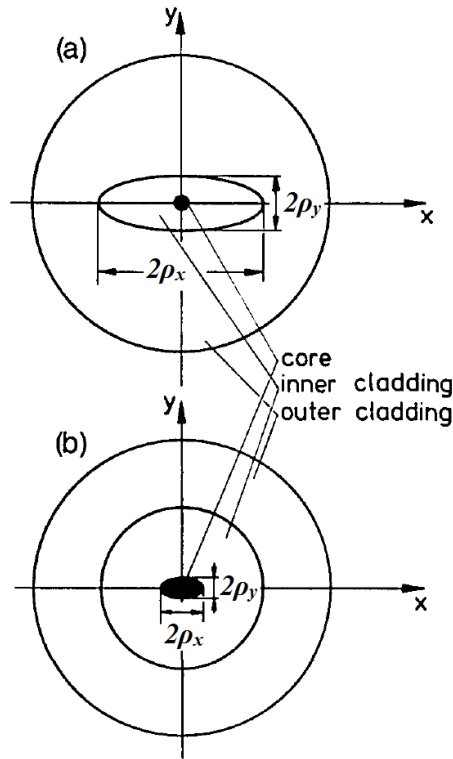


Figure 3.11 “Cross section of fibers with elliptical structure. (a) Round core in an elliptical inner cladding. (b) Elliptical core in a round cladding.” [20]

For the first case (Figure 3.11 a), the birefringence is modeled as

$$\delta\beta_{stress\ e clad} = \beta_x - \beta_y = \frac{k_0}{2} n^3 (p_{11} - p_{12}) \times \frac{(\alpha_{ocl} - \alpha_{icl})(T_{soft} - T_{room})}{1 - N^2} \times \frac{\rho_x - \rho_y}{\rho_x + \rho_y}$$

or

$$\delta\beta_{stress\ e clad} = \frac{k_0}{2} n^3 (p_{11} - p_{12}) \times \frac{(\alpha_{ocl} - \alpha_{icl})(T_{soft} - T_{room})}{1 - N^2} \times \frac{e_{clad}}{(1 + \sqrt{1 - e_{clad}})^2}$$
(3.5)

Here n denotes the mean refractive index, p_{11} and p_{12} are the components of the photoelastic tensor, α_{ocl} and α_{icl} are the thermal-expansion coefficients of the outer and inner cladding respectively, T_{soft} and T_{room} are the softening temperature of the fiber material and the room temperature respectively, N is the Poisson's ratio of the fiber material and e_{clad} is the inner cladding ellipticity..

For the second case (Figure 3.11 b), the birefringence is given by

$$\delta\beta_{stress\ e core} = \beta_x - \beta_y = \left(1 - \frac{U^2}{V^2}\right) \times \frac{k_0}{2} n^3 (p_{11} - p_{12}) \times \frac{(\alpha_{icl} - \alpha_{core})(T_{soft} - T_{room})}{1 - N^2} \times \frac{\rho_x - \rho_y}{\rho_x + \rho_y}$$

or

$$\delta\beta_{stress\ e core} = \left(1 - \frac{U^2}{V^2}\right) \times \frac{k_0}{2} n^3 (p_{11} - p_{12}) \times \frac{(\alpha_{icl} - \alpha_{core})(T_{soft} - T_{room})}{1 - N^2} \times \frac{e}{(1 + \sqrt{1 - e})^2}$$
(3.6)

The following graph displays the dependence of the birefringence on the normalized frequency in both cases.

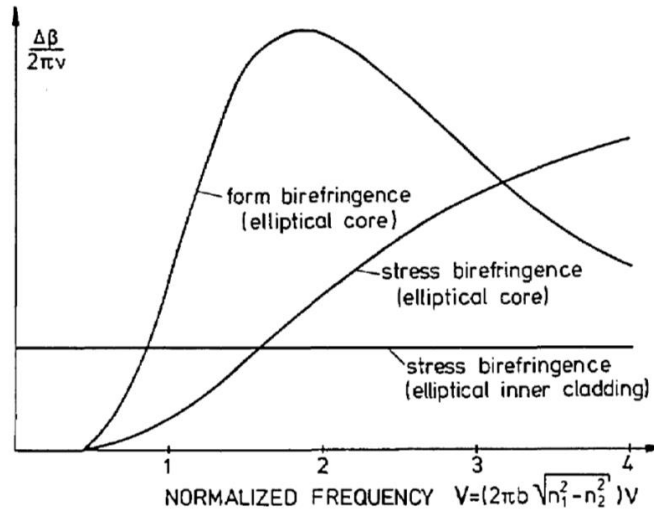


Figure 3.12 “Frequency dependence of the three kinds of linear birefringence” [20]

3.2.3 Birefringence due to bends [21]

Often fibers are bent around drums, solid objects or experience microbending, leading to bending induced birefringence. Ulrich et al. [21] concluded that this type of birefringence results from stresses. A bent fiber experiences tensile stress in its outer layers with respect to the central axis of the fiber and a compressive stress in the inner layers with respect to the same axis (see Figure 3.13). Although these stresses generate birefringence, they don't contribute directly to it; only second order dependence causes the birefringence.

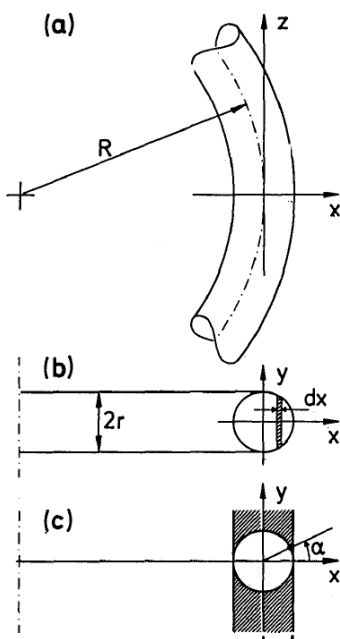


Figure 3.13 “Geometry of a bent fiber” [21]

For an elastically homogeneous and isotropic fiber the birefringence associated with bending a fiber around a drum, with a bending radius R equals

$$\delta\beta_{bend} = \beta_x - \beta_y = \frac{k_0 n_c^3}{4} \times (p_{11} - p_{12}) \times (1 + N) \times \frac{r^2}{R^2} \quad (3.7)$$

in which $2r$ is the outer diameter of the fiber (All other variables are the same as discussed in previous sections). Figure 3.14 shows the agreement of equation (3.7) to some measurement of [21] and displays the proportionality between the bending-induced birefringence and the outer fiber diameter.

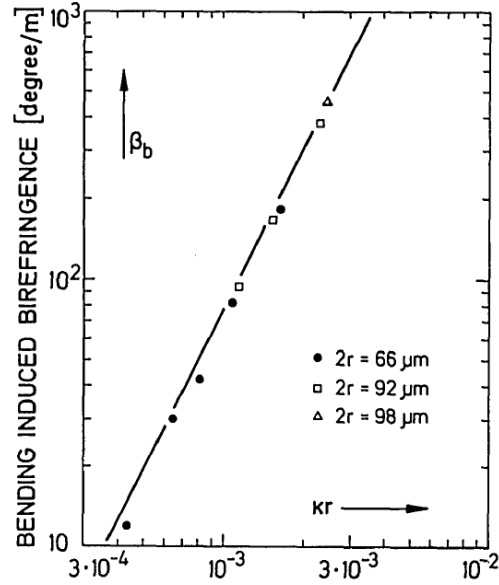


Figure 3.14 “Bending birefringence of single-mode silica fibers. The solid line represents the calculated birefringence (3.7). The points are measurements at 0.633 and 0.676 μm using three fibers of different origins. ($\kappa=1/R$)” [21]

3.2.4 Birefringence due to bends under tension [22]

Although fiber bends and tensile stresses do not generate birefringence to first order due to cylindrical fiber symmetry, the combination of bending and tensile stress yields birefringence to first order. Hence if either bending or curvature is removed, this component of birefringence is null. With the directions of the fiber and the coil axis defined as in Figure 3.15, the birefringence generated by the combination of tension and bending denoted β_{tc} is given by

$$\delta\beta_{tc} = \beta_x - \beta_y = \frac{k_0 n_{eff}^3}{2} \times (p_{11} - p_{12}) \times \frac{(1+N) \times (2-3N)}{1-N} \times \frac{r}{R} \times \varepsilon_z \quad (3.8)$$

Here n_{eff} is the effective refractive index and ε_z is the axial strain (All other variables are the same as discussed in previous sections). Figure 3.16 shows some measured data indicating done by Rashleigh and Ulrich proving the validity of equation(3.8).

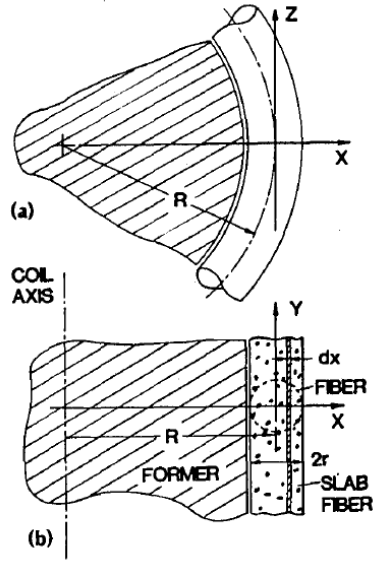


Figure 3.15 “Geometry of a tension-coiled fiber” [22]

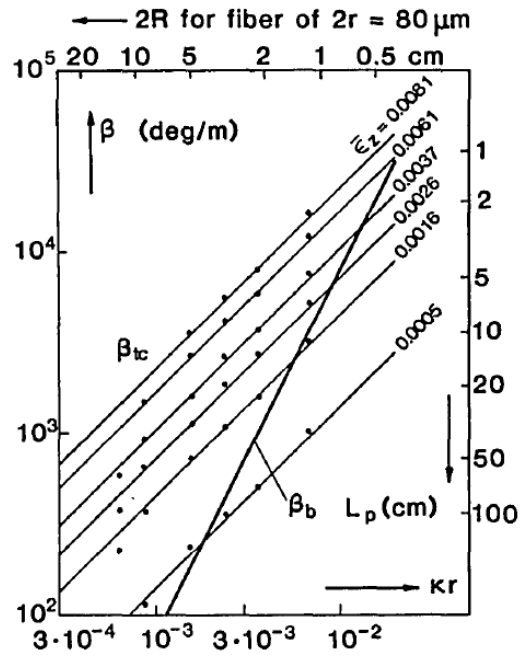


Figure 3.16 “Tension-coiled birefringence β_{tc} of single-mode fibers. The solid lines represent the calculated birefringence. Measurements for $\lambda = 0.633 \mu\text{m}$ are indicated by the dots. ($\kappa = 1/R$)” [22]

3.2.5 Birefringence due to twists [23]

In chapter 11 and Appendix E of [23], Chin-Len Chen discusses the birefringence due to fiber twists. Although previous types of birefringence are linear, twists cause circular birefringence. If a fiber of length L is twisted by an angle Θ (positive when twisted counter clockwise) the resultant birefringence $\delta\beta_{TW}$ due to twists is

$$\delta\beta_{TW} = \beta_R - \beta_L = \frac{n_c^2}{2} \times (p_{11} - p_{12}) \times \frac{\Theta}{L} \times F_{TW}(V) \quad (3.9)$$

in which, β_R and β_L are the propagation constant of the right- and left-hand circularly polarized modes, and $F_{TW}(V)$ is a function of the normalized frequency V .

Chapter 4

Dispersion Compensation Modules (DCMs) behavior under temperature variations

In this chapter we examine the variation of the Differential Group Delay (DGD) of a DCM with temperature variations in a controlled setup.

4.1 THE EXPERIMENT

4.1.1 Setup Description

We investigate a Nortel DSCM-10A, part no: 0121.0101 DCM by placing the device in a box and further thermally isolating it with fiberglass. We then connect two thermal modules in to the DCM with a thermal paste and attach four thermal sensors in contact with DCM to measure its temperature at four different points. Each thermal module and the 2 sensors are connected to a temperature controller.

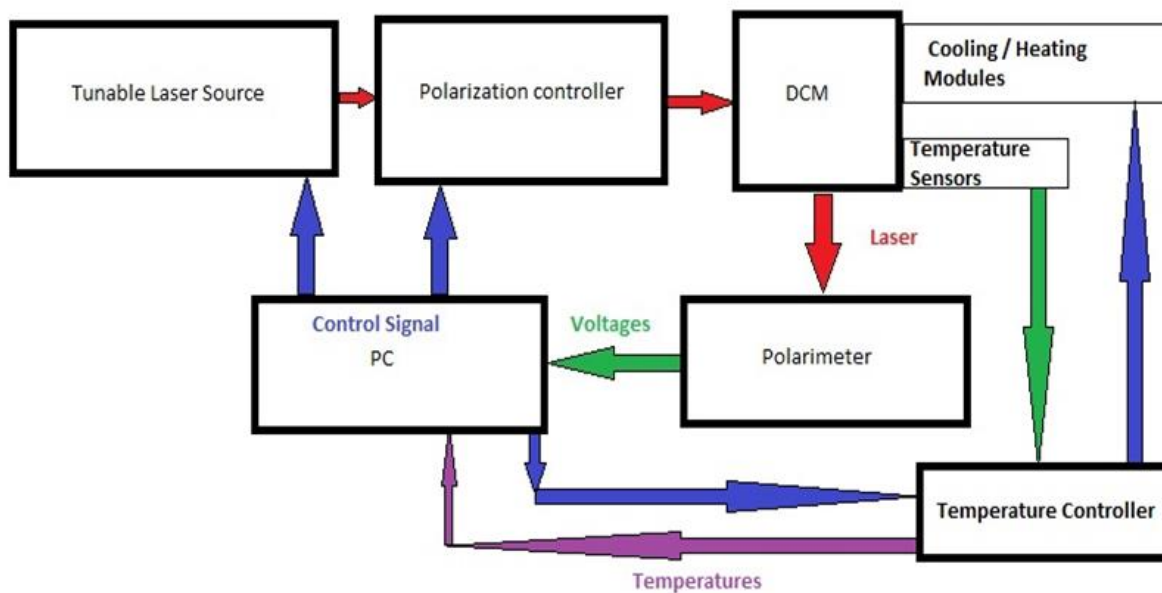


Figure 4.1 Setup block diagram, showing signals and laser flows.

The DCM is excited by a tunable laser followed by a polarization controller while the output of the DCM is input into a polarimeter. A lab computer controls the 2 temperature controllers, the tunable laser source, and the polarization controller and acquires the polarimeter readings (Figure 4.1).

4.1.2 Experiment Procedure

A Matlab program sets the desired temperature via the temperature controllers. After the temperature is stabilized, the program enables the tunable laser source and sets the polarization

controller to a random polarization; then the polarimeter transforms the output polarization to four voltages read by the PC. The voltages acquired by the polarimeter can be used to calculate the S-parameters of the output polarization via a conversion matrix characterizing the polarimeter. To be able to calculate a DGD point, we need to measure three different output polarization points at two different wavelengths as explained in Section 1.5.

4.2 Results

4.2.1 DCM under room temperature effect

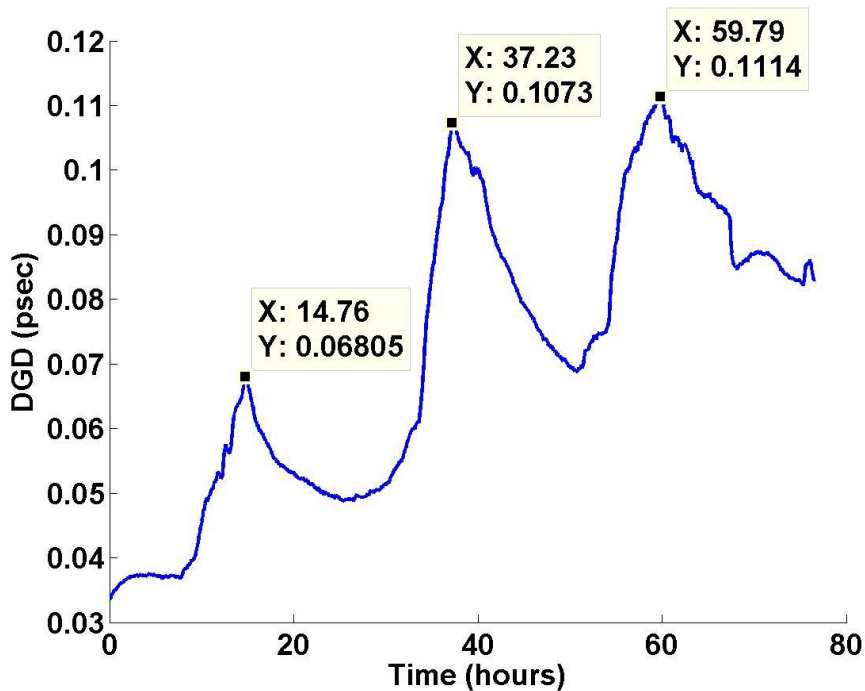


Figure 4.2 DGD evolution in room temperature for 76.5 hours

As the room temperature fluctuates throughout the day, the DCM's DGD is affected. Figure 4.2 shows the DGD variations during a period of approximately 3 days. The curve exhibits a 24 hour period resulting from daily temperature changes, as already noted in Section 3.1.2 [15]. The anomalous behavior of the first cycle is associated with the 36° initial temperature of the DCM.

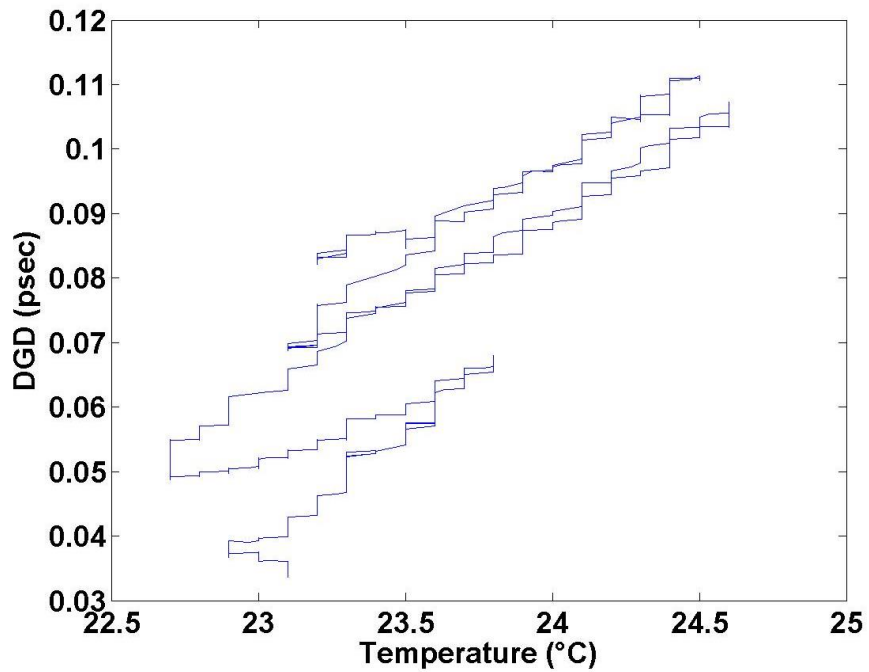


Figure 4.3 DGD vs. Room Temperature

Figure 4.3 displays DGD versus temperature which is similar to [13] and [24] measured data.

4.2.2 DCM's DGD vs. Temperature

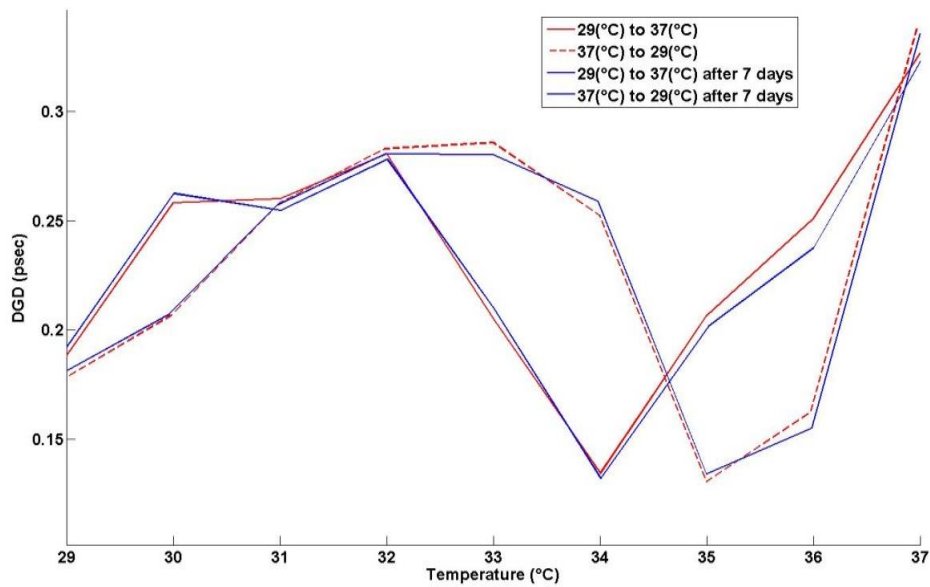


Figure 4.4 Reproducible curves under same circumstances

Although the previous measurements of [15] and [24] appear to indicate that the DGD versus temperature curves are determined solely by the DCM's temperature, however Figure 4.4 demonstrates that the DGD obtained when heating the DCM (solid curves) is different than that obtained when the DCM is cooled (dotted curves). Further, when this measurement was repeated a week later (blue and red curves), the same traces were reproduced; which doesn't comply with the Maxwellian randomness of the DGD! [25]. Furthermore, Figure 4.5 demonstrates that the heating and cooling process yields different DGD curves if the curves start at 26° Celsius and end at different temperatures (34°, 35°, 36° and 37° Celsius) before returning to 26°C. Only curves varying from 26° to 37°C were reproduced, when compared to Figure 4.4 (blue curves).

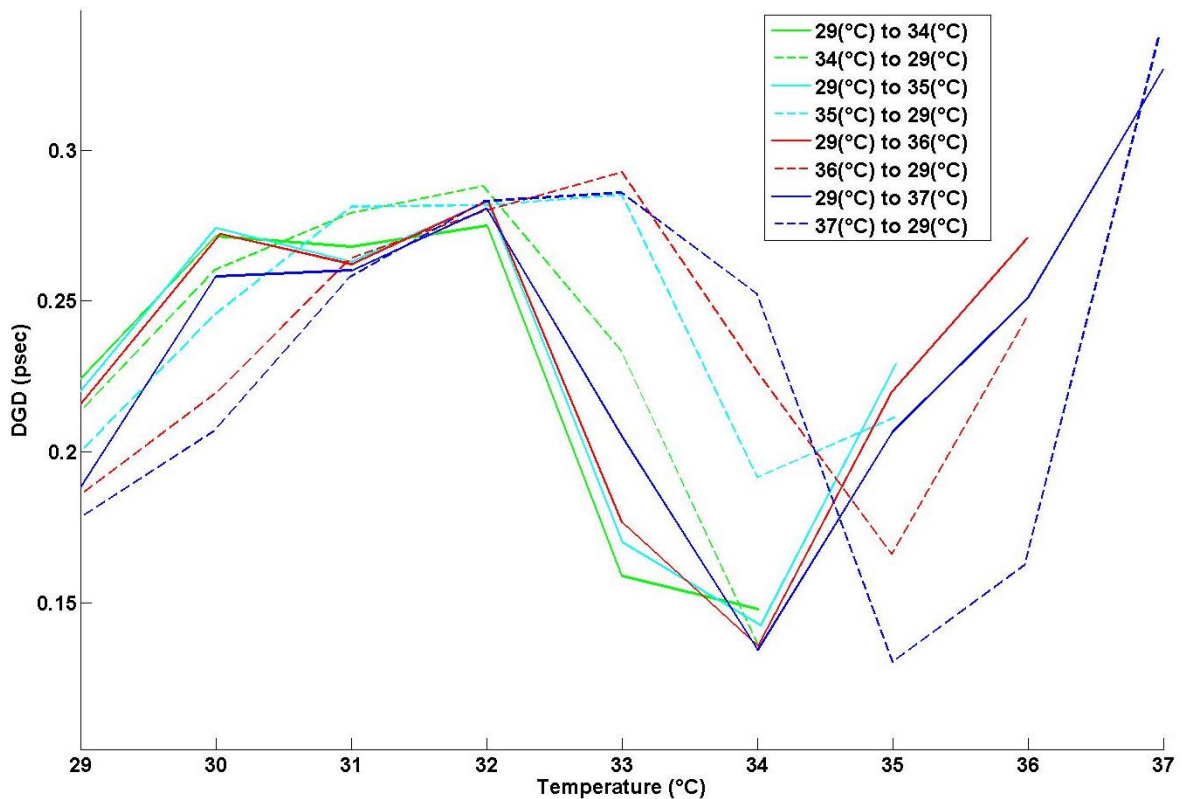


Figure 4.5 Irreproducible curves of DGD vs. Temperature at different Temperatures ranges

Additionally, Figure 4.6 shows that if we add a delay of 6 hours between every temperature change (red curves) and compare the new curves with the old ones (blue curves), these traces do not coincide as in Figure 4.4.

These measurements show that unless all circumstances, which are initial and final temperatures, timing between successive temperatures and increasing or decreasing the temperature are identical, measuring reproducible DGD curves is not possible. Hence temperature is not the only parameter controlling the DGD despite the strong correlation between both of them.

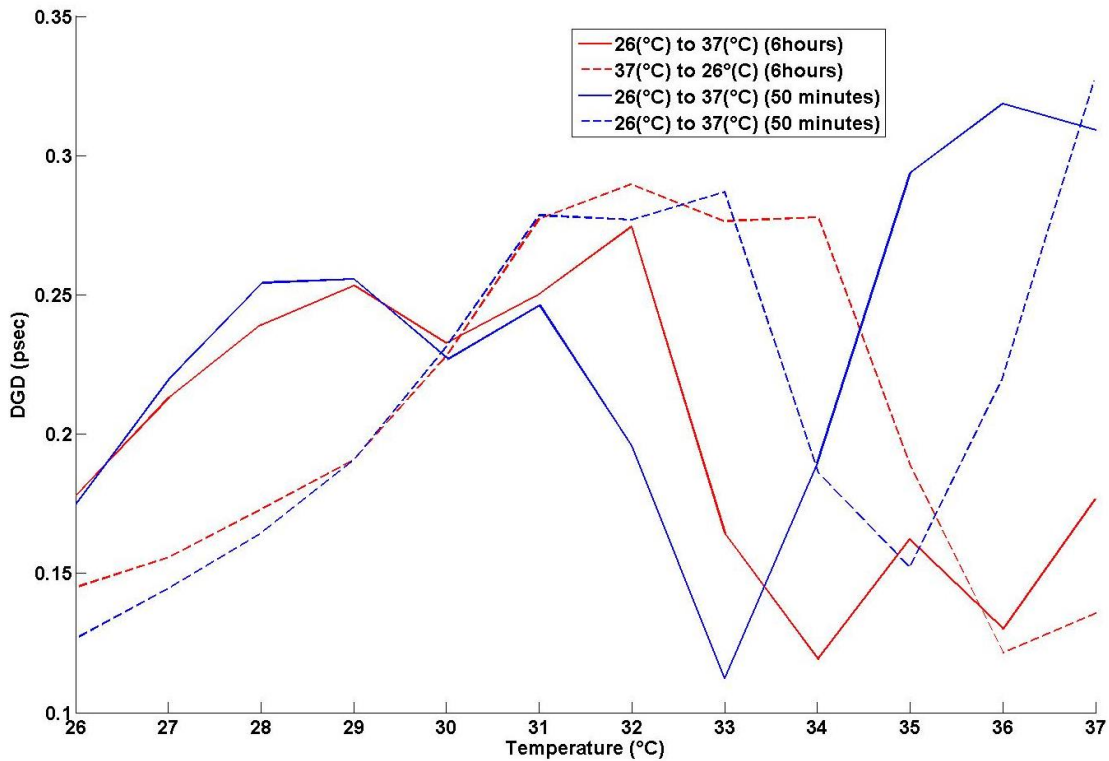


Figure 4.6 Irreproducible curves of DGD and Temperature different settling times

4.2.3 Hysteresis and temperature spans

Although we demonstrated the correlation of many parameters to the DGD in the previous section, the DGD behavior is dependent on the temperature extremes (Figure 4.7.1 and Figure 4.8.1). By comparing the behavior of the DGD in all three cases –Figure 4.7.1, Figure 4.8.1 and Figure 4.9.1 – we conclude that the DGD of the fiber-based DCM depends on the history of its temperature evolution and that this effect becomes more relevant with increased temperature variation. Plotting the absolute difference between the DGDs, for cooling and heating for each set of curves (Figure 4.7.2, Figure 4.8.2 and Figure 4.9.2), shows that the wider the span of temperature the higher the difference between cooling and heating curves, provided that the circumstances are the same.

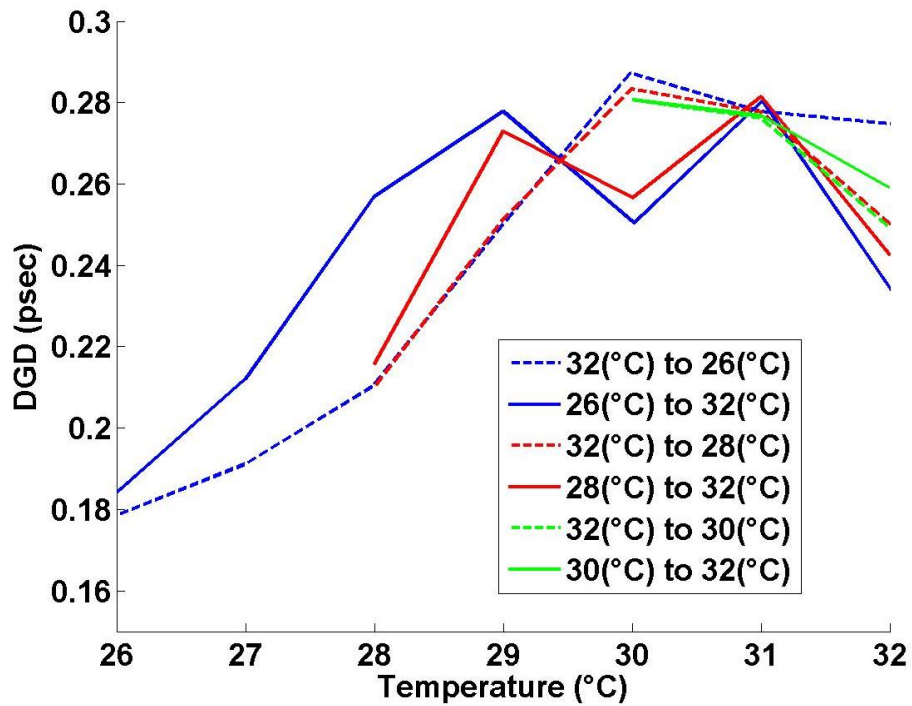


Figure 4.7.1 The DGD measured when heating (Solid lines) and cooling (Dotted lines) the DCM from different starting temperatures to 32°C.

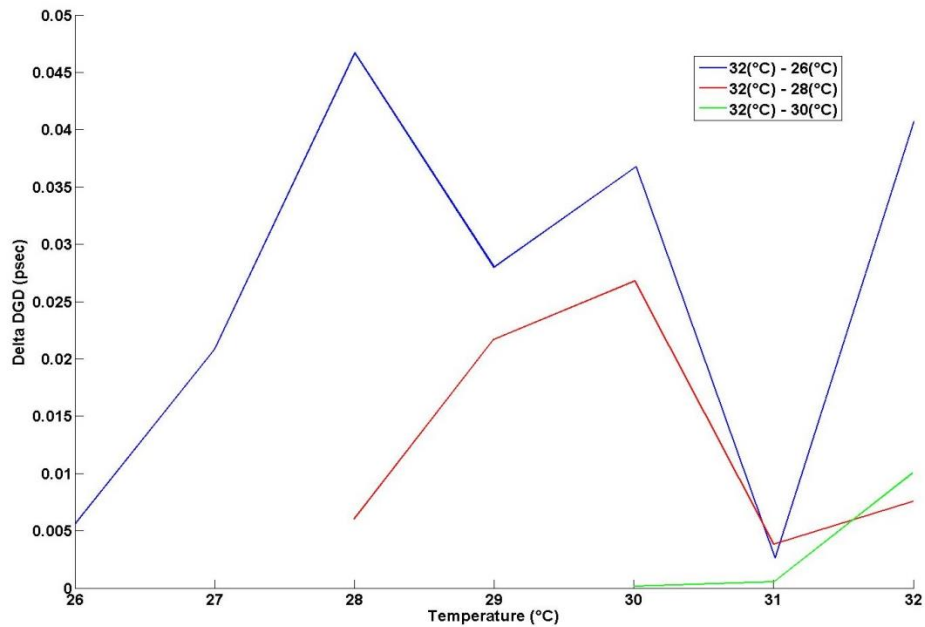


Figure 4.7.2 Divergence between heating and cooling measurements for the curves in the above figure.

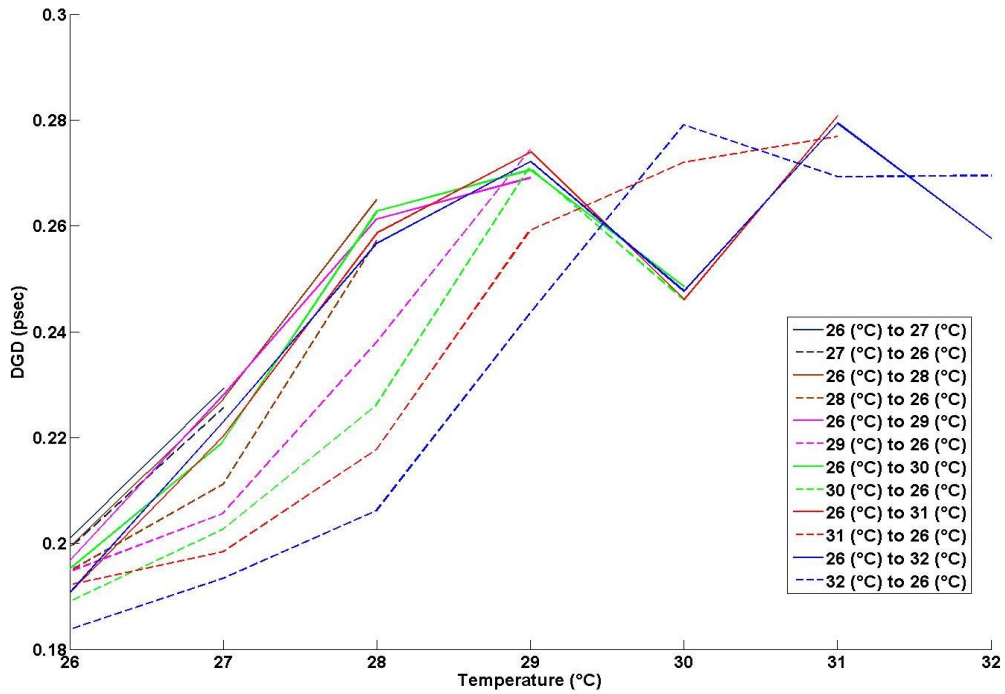


Figure 4.8.1 Heating (Solid lines) and cooling (Dotted lines) measurements with a minimum of 26°C and maximum variable temperatures.

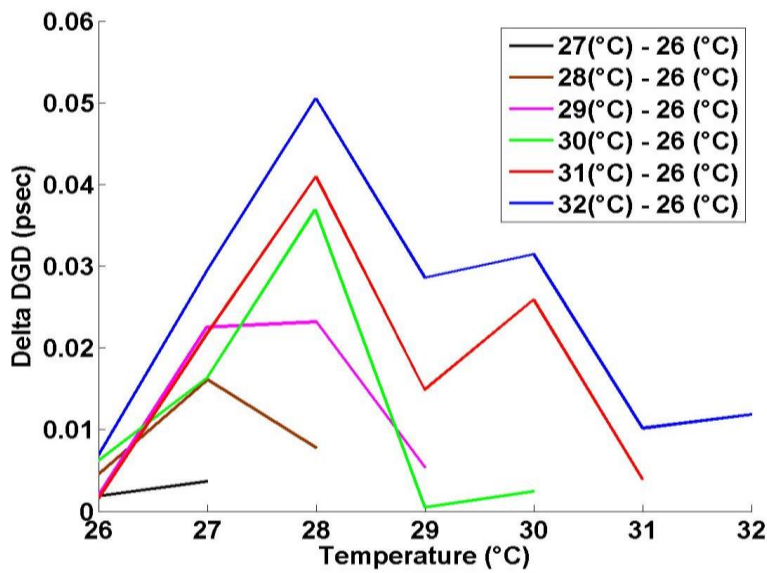


Figure 4.8.2 Divergence between heating and cooling measurements for the curves in the above figure.

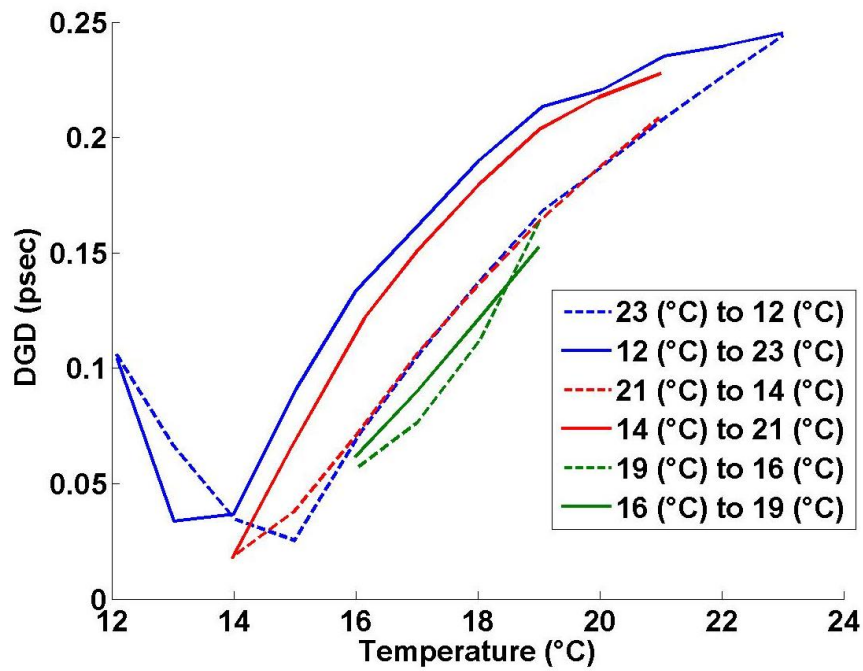


Figure 4.9.1 Heating (Solid lines) and cooling (Dotted lines) measurements with variable maximum and minimum temperatures.

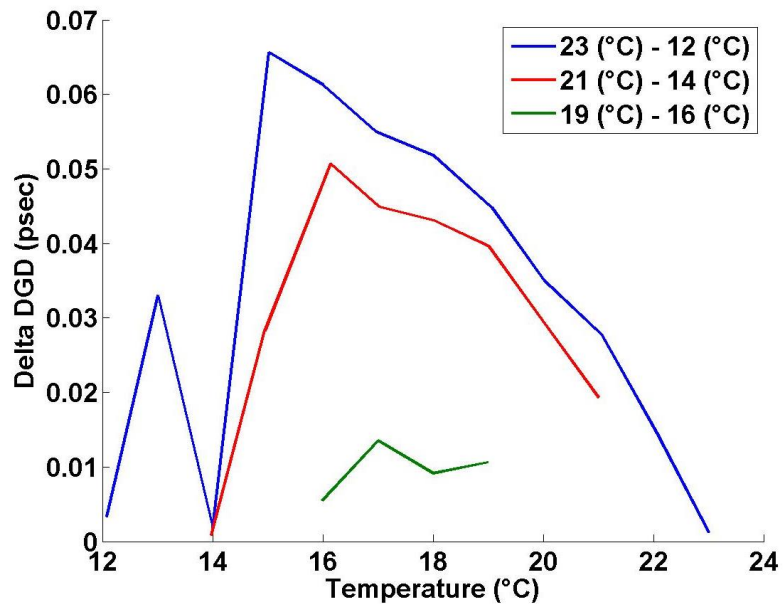


Figure 4.9.2 Divergence between heating and cooling measurements for the curves in the above figure.

4.2.4 DGD relaxation with time

Ramaswamy et al. observed a birefringence relaxation with time in optical fibers that takes days to return an initial value [26]. To illustrate the relaxation of the DGD with time, Figure 4.10 shows the measured DGD as a function of time at different temperatures. A DGD relaxation is observed every time the temperature is changed. This relaxation appears to have an impact on the initial DGD value of the successive temperature. The small DGD features superimposed on the relaxation curves are the result of small temperature variations ($\sim 0.1^\circ\text{C}$) (Figure 4.11).

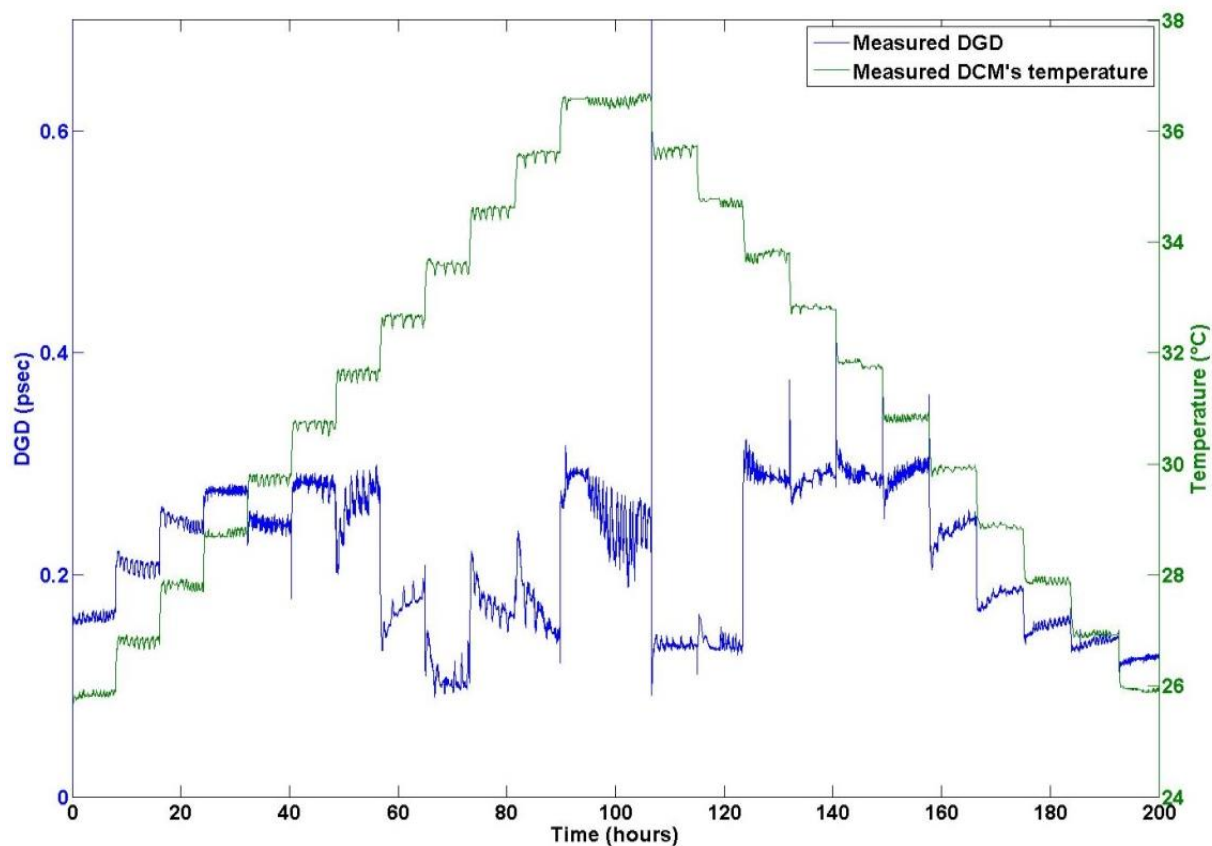


Figure 4.10 DGD vs. Time at different temperatures (8 hours per temperature)

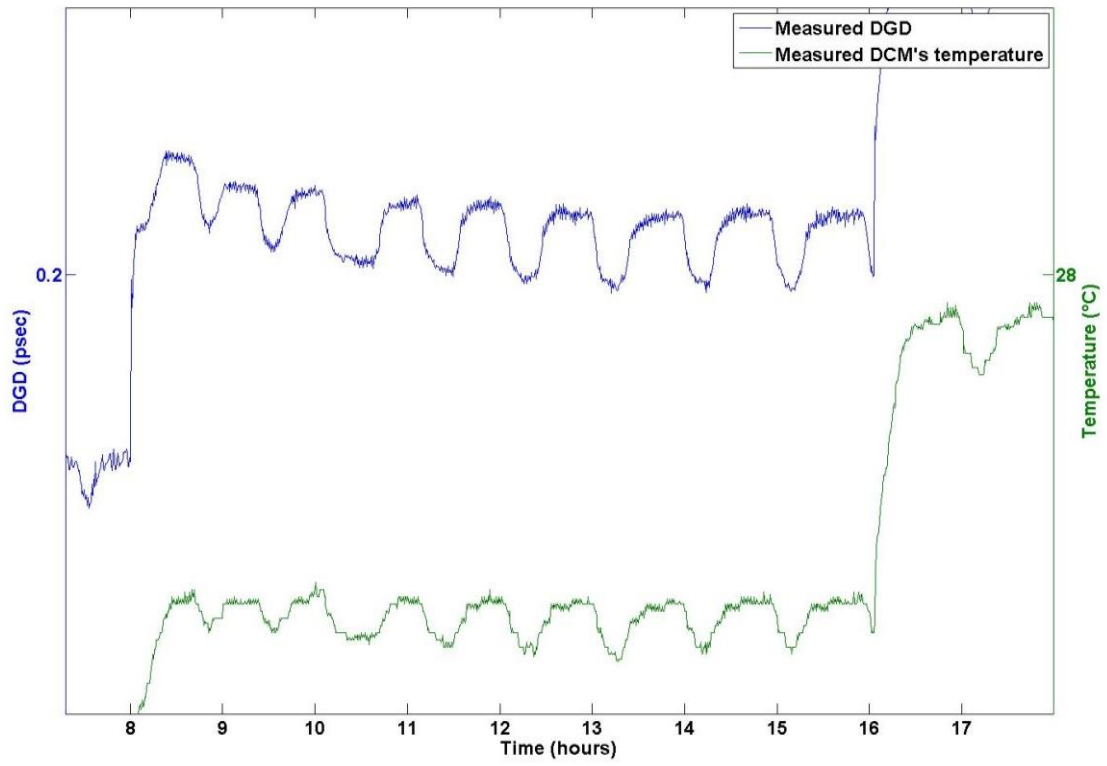


Figure 4.11 DGD vs. Time during the second temperature cycle displayed in the previous figure.

Chapter 5

Modeling the DCM

In this chapter we introduce a mathematical model of the single-mode fiber-based DCM tested previously and whose fiber is coiled in a cylindrical form and placed in a temperature controlled chamber. We employ the mathematical techniques of the first three chapters to qualitatively explain the measurements in Chapter 4. Although, the model is the first to include mechanical relaxation in DGD predictions, it assumes that shear stresses are negligible as the fiber doesn't suffer deformations at varying room temperature. Perturbation length theory [27] [28] is also taken into account in this model.

5.1 Fiber-based DCM's strain model

We model the strain in the DCM by a constant value ($\varepsilon_{total} = \varepsilon_0$) as the fiber inside the DCM is glued to the outside of the drum and therefore is not displaced physically as the temperature changes. The strain component generated by stress contributes to the birefringence generated by the coiling of the fiber under tension as discussed in section 3.2.4. Rearranging equation(2.15), the elastic strain is expressed as follows

$$\begin{aligned} \varepsilon^E(t) &= \varepsilon_0 - \varepsilon_f(t) - \varepsilon^D(t) \\ \varepsilon^E(t) &= \varepsilon_0 - \alpha_{icl}(T(t) - T_0) - \int_0^t \frac{\sigma(t')}{\eta_V} e^{-(t-t')/\tau_D} dt' \end{aligned} \quad (5.1)$$

where T_0 is a constant temperature and $T(t)$ is the DCM's temperature as a function in time. From equation(2.11), (5.1) can be written as follows

$$\varepsilon^E(t) = \varepsilon_0 - \alpha_{icl}(T(t) - T_0) - \int_0^t \frac{3K_1}{\eta_V} \varepsilon^E(t') e^{-(t-t')/\tau_D} dt' \quad (5.2)$$

which is a linear Volterra integral equation that can be solved by Laplace transform. Written as

$$x(t) = g(t) - \int_0^t x(t') k(t-t') dt' \quad (5.3)$$

where

$$\begin{aligned} x(t) &= \varepsilon^E(t) \\ g(t) &= \varepsilon_0 - \alpha_{icl}(T(t) - T_0) \\ k(t) &= \frac{3K_1}{\eta_V} e^{-t/\tau_D} \end{aligned} \quad (5.4)$$

taking the Laplace transform of (5.3) yields

$$X(s) = G(s) - X(s) K(s) \quad (5.5)$$

Hence

$$X(s) = G(s) \frac{1}{1 + K(s)} \quad (5.6)$$

where

$$K(s) = \frac{3K_1}{\eta_V} \frac{\tau_D}{1 + s\tau_D} \quad (5.7)$$

Then

$$\begin{aligned} X(s) &= G(s) \frac{1}{1 + \frac{3K_1}{\eta_V} \frac{\tau_D}{1 + s\tau_D}} = G(s) \frac{\eta_V/3K_1(1 + s\tau_D)}{\eta_V/3K_1(1 + s\tau_D) + \tau_D} \\ &= G(s) \frac{\eta_V/3K_1(1 + s\tau_D) + \tau_D - \tau_D}{\eta_V/3K_1(1 + s\tau_D) + \tau_D} \\ &= G(s) \left[1 - \frac{\tau_D}{\eta_V/3K_1 + s\tau_D\eta_V/3K_1 + \tau_D} \right] \\ &= G(s) \left[1 - \frac{1}{\eta_V/3\tau_D K_1 + 1 + s\eta_V/3K_1} \right] \end{aligned} \quad (5.8)$$

From equation (2.14)

$$X(s) = G(s) - G(s) \frac{3K_1/\eta_V}{3(K_1 + K_2)/\eta_V + s} \quad (5.9)$$

An inverse Laplace transform yields

$$x(t) = g(t) - \frac{3K_1}{\eta_V} \int_0^t g(t') e^{-(t-t')/\tau_r} dt' \quad (5.10)$$

with

$$\tau_r = \frac{\eta_V}{3(K_1 + K_2)} \quad (5.11)$$

Hence the elastic strain as a function of time is

$$\varepsilon^E(t) = \left[\varepsilon_0 - \alpha_{icl} (T(t) - T_0) \right] - \frac{3K_1}{\eta_V} \int_0^t \left[\varepsilon_0 - \alpha_{icl} (T(t') - T_0) \right] e^{-(t-t')/\tau_r} dt' \quad (5.12)$$

5.2 Physical parameters and mathematical equations

In this section, we present the constants, parameters and equations employed in our simulation of the DCM. In Table 5-1 we present constants and parameters for a typical single-mode fiber in the DCM. The operating wavelength and the radius of curvature are measured values, while the fiber length is estimated from the DCM properties. The outer fiber radius is taken as a typical cladding radius; the later postulate was assumed to agree with Ulrich et al. postulate stating that the fiber is elastically homogeneous and isotropic to validate the use of their formulation (section 3.2.3, [21]). We further assume that the stresses induced by the plastic jacket around the fiber can be neglected. Although the ellipticity is chosen to be zero in this model to fit the previously measured DGD curves, we will include its formulas in the mathematical model to present a complete DGD model.

Table 5-1 Physical parameters characterizing the fiber-based DCM (SI units)

Symbo l	Parameter name	Value
λ	Operating wave-length	$1.55 \times 10^{-6} (m)$
$\delta\lambda$	Differential wave length	$2 \times 10^{-9} (m)$
n_c	Core refractive index	1.44402 [29]
n_{cl}	Clad refractive index	1.4388 [29]
ρ	Core mean radius	$4.1 \times 10^{-6} (m)$ [29]
e	Core ellipticity	0
p_{11}	Component of photoelastic tensor	0.126 [29]
p_{12}	Component of photoelastic tensor	0.260 [29]
α_{icl}	Thermal-expansion coefficient of inner cladding	$5.6 \times 10^{-7} (^{\circ}C^{-1})$ [29]
α_{core}	Thermal-expansion coefficient of core	$9.19 \times 10^{-7} (^{\circ}C^{-1})$ [29]
T_{room}	Room temperature	26 - 37($^{\circ}C$)
T_{soft}	Softening temperature of Silica (fiber material)	1065($^{\circ}C$) [29]
N	Poisson ratio of silica	0.17 [23]
R	Radius of curvature of the coiled-fiber (DCM)	$8.75 \times 10^{-2} (m)$
r	Outer radius of the DCM's fiber	$125 \times 10^{-6} (m)$
L	Fiber length	$\sim 5000 (m)$
E	Young's Modulus	$\sim 68 \times 10^9 (Pascal)$ [7] [8]
η_V	Volume Viscosity	$\sim 5 \times 10^{20}$ ([6] page 150)

The Young's Modulus and the volume viscosity are as well assigned the values above in consistence with the observed data as no direct measurements appear to exist for these quantities at room temperature (Section Figure 2.3).

5.2.1 Single section general model

In Table 5-2 we present the equations we employ to calculate the propagation constants of the fiber for each section. The core and clad parameters are obtained from the defining equations(3.4), through numerical iteration.

Table 5-2 Relations used to obtain fiber parameters

order	Equation	Equation #
Relative refractive index	$\Delta = \frac{n_c^2 - n_{cl}^2}{2n_c^2}$	(3.3)
Normalized frequency	$V = \frac{2\pi}{\lambda} \rho n_c \sqrt{2\Delta} = k_0 \rho n_c \sqrt{2\Delta}$	(3.3)
Core, clad parameters and propagation constant	$U \frac{J_{-1}(U)}{J_0(U)} = -W \frac{K_{-1}(W)}{K_0(W)}$ $U = \rho \sqrt{k_0^2 n_c^2 - \beta^2}$ $W = \rho \sqrt{\beta^2 - k_0^2 n_{cl}^2}$ $\rho(k_0^2 n_c^2 - k_0^2 n_{cl}^2) = U^2 + W^2$	(3.4)

In Table 5-3 we collect the equations of Section 3.2, which form the basis of our numerical model. We also assume that the simulated fiber has a single clad.

Table 5-3 Mathematical model of the fiber-based DCM

order	Equation	Equation #
Geometrical deformation birefringence	$\delta\beta_G = \frac{e^2 (2\Delta)^3}{\rho} \frac{W^2}{8V^3} \left[U^2 + (U^2 - W^2) \left\{ \frac{J_0(U)}{J_1(U)} \right\}^2 + U W^2 \left\{ \frac{J_0(U)}{J_1(U)} \right\}^3 \right]$	(3.2)
Built-in stress birefringence	$\delta\beta_{stress\ ecore} = \left(1 - \frac{U^2}{V^2}\right) \times \frac{k_0 n^3}{2} (p_{11} - p_{12}) \times \frac{(\alpha_{icl} - \alpha_{core})(T_{soft} - T_{room})}{1 - N^2} \times \frac{e}{(1 + \sqrt{1 - e})^2}$	(3.6)
Bend's birefringence	$\delta\beta_{bend} = \beta_x - \beta_y = \frac{k_0 n_c^3}{4} \times (p_{11} - p_{12}) \times (1 + N) \times \frac{r^2}{R^2}$	(3.7)
Tension-coiled birefringence	$\delta\beta_{tc} = \frac{k_0 n_{eff}^3}{2} \times (p_{11} - p_{12}) \times \frac{(1 + N) \times (2 - 3N)}{1 - N} \times \frac{r}{R} \times \varepsilon_z$	(3.8)
Elastic strain	$\varepsilon^E(t) = [\varepsilon_0 - \alpha_{icl}(T(t) - T_0)] - \frac{3K_1}{\eta_V} \int_0^t [\varepsilon_0 - \alpha_{icl}(T(t') - T_0)] e^{-(t-t')/\tau_r} dt'$	(5.12)

The constant ε_z in (3.8) equals to ε^E of (5.12). To calculate ε^E , we assume that the initial strain ε_0 is given by

$$\varepsilon_0 = \frac{\text{stress}}{\text{Young's Modulus}} = \frac{F/\pi r^2}{E} \quad (5.13)$$

where F is the initial applied force, assumed to be 0.95 (N), during manufacturing at room temperature (T_0 of 25° Celsius).

In order to calculate τ_r and K_1 one of these 2 variables must be assigned a representative value. Hence τ_r is assumed to be equal 14.3 hours (51480 seconds) after which the following set of equations yield K_1 . From (2.16)

$$\frac{1}{K} = \frac{1}{K_1} + \frac{1}{K_2} = \frac{1}{xK} + \frac{1}{yK} \quad (5.14)$$

where

$$K_1 = xK, \quad K_2 = yK \quad (5.15)$$

and

$$1 = \frac{1}{x} + \frac{1}{y} \Rightarrow x + y = xy \quad (5.16)$$

while equation (5.11) yields

$$x + y = \frac{\eta_v}{3K\tau_r} \quad (5.17)$$

$$\therefore x + y = xy = \frac{x}{1 - 1/x}$$

$$\therefore \frac{\eta_v}{3K\tau_r} = \frac{x^2}{x-1} \quad (5.18)$$

$$x^2 - \frac{\eta_v}{3K\tau_r}x + \frac{\eta_v}{3K\tau_r} = 0$$

so that

$$x = \frac{\frac{\eta_v}{3K\tau_r} + \sqrt{\left(\frac{\eta_v}{3K\tau_r}\right)^2 - 4\frac{\eta_v}{3K\tau_r}}}{2} \quad (5.19)$$

Given x , and hence K_j , the strain can be evaluated.

5.2.2 Total DGD of the system

After employing the above equations in the previous section to calculate the birefringence of a single section, we apply the concatenated sections model of Section 1.3 to determine the total DGD. The length of each section set equal to the autocorrelation length which corresponds to the distance after which the fiber loses memory of the direction of the initial axis of birefringence [28] as the birefringence axes of each section are oriented randomly with respect to each other. From the measurements of [27] of the autocorrelation length of different samples of a single-mode step-index fiber we here employ a length of 25 meters which is slightly longer than the lengths cited in this publication. This yields a system of 200 concatenated sections (for a 5 Km fiber) with randomly oriented slow PSP axes.

In order to determine the Jones matrix of the series of concatenated sections from the birefringence of each section, we employ the Jones matrices technique described in section 1.4. The system's DGD is obtained by relating the output polarization at certain frequency (ω) and the output at an adjacent frequency ($\omega + \Delta\omega$) using the Jones space. From equation(1.5),

$$\begin{aligned} |v\rangle_\omega &= U_\omega |s\rangle \\ |v\rangle_{\omega+\Delta\omega} &= U_{\omega+\Delta\omega} |s\rangle \end{aligned} \quad (5.20)$$

where the input polarization $|s\rangle$ is independent of the angular frequency ω , and therefore,

$$U_{\omega+\Delta\omega} = U_\omega + U'_\omega \Delta\omega \quad (5.21)$$

Accordingly

$$|v\rangle_{\omega+\Delta\omega} = (U_\omega + U'_\omega \Delta\omega) |s\rangle = (U_\omega + U'_\omega \Delta\omega) U_\omega^{-1} |v\rangle_\omega \quad (5.22)$$

$$|v\rangle_{\omega+\Delta\omega} = (I + U'_\omega U_\omega^{-1} \Delta\omega) |v\rangle_\omega = U_{\omega+\Delta\omega} U_\omega^{-1} |v\rangle_\omega \quad (5.23)$$

Consequently, the total Jones matrix of the system U_T

$$U_T = U_{\omega+\Delta\omega} U_\omega^{-1} = (I + U'_\omega U_\omega^{-1} \Delta\omega) \quad (5.24)$$

from which, according to equation (1.22), the system's total DGD is

$$\frac{\tau_{system}^2}{4} = \det(U'_\omega U_\omega^{-1}) = \det\left(\frac{U_T - I}{\Delta\omega}\right) \quad (5.25)$$

and hence

$$\tau_{system} = 2 \times \sqrt{\det\left(\frac{U_T - I}{\Delta\omega}\right)} \quad (5.26)$$

5.3 Numerical results

We first discuss the results of the numerical model presented above employing the values presented in Table 5-1. With an appropriate randomly oriented set of PMD vectors, we obtained the curves of Figure 5.1 which agree with the experimental measurements in Figure 4.4, Figure 4.10 and Figure 4.11. The temperature variation as a function of time is taken to be that measured in Section 4.2.4. A period of 5 days is incorporated at the beginning of the simulation to ensure that the initial transient elastic strain was sufficiently relaxed. Figure 5.1 shows the averaged simulated and measured DGD during a heating and cooling cycle; while Figure 5.2 shows the same simulated and measured DGD and temperature versus time; and Figure 5.3 is a detailed view for the second heating cycle of Figure 5.2. The curves clearly indicate the manner in which temperature variations influence DGD. The agreement between the measured and simulated DGD indicate that the mechanical stress relaxation associated with the viscoelasticity of glass results in the observed DGD changes when the temperature fluctuates around an average temperature.

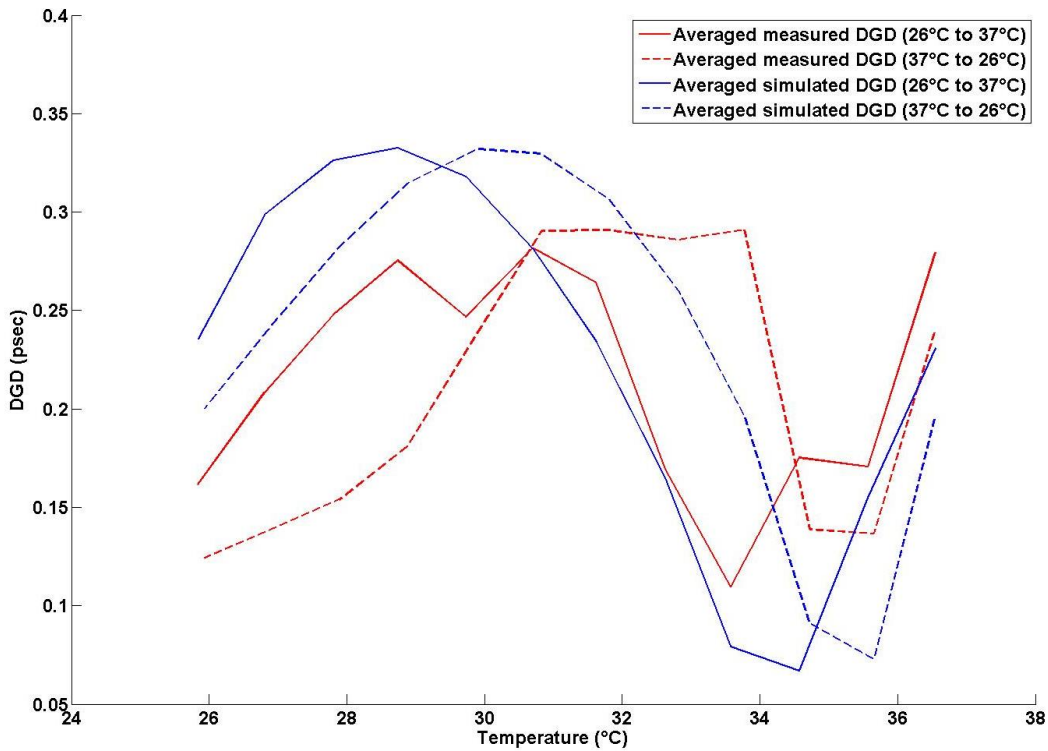


Figure 5.1 Averaged measured DGD (red curves) and Simulated DGD (blue curves) versus Temperature

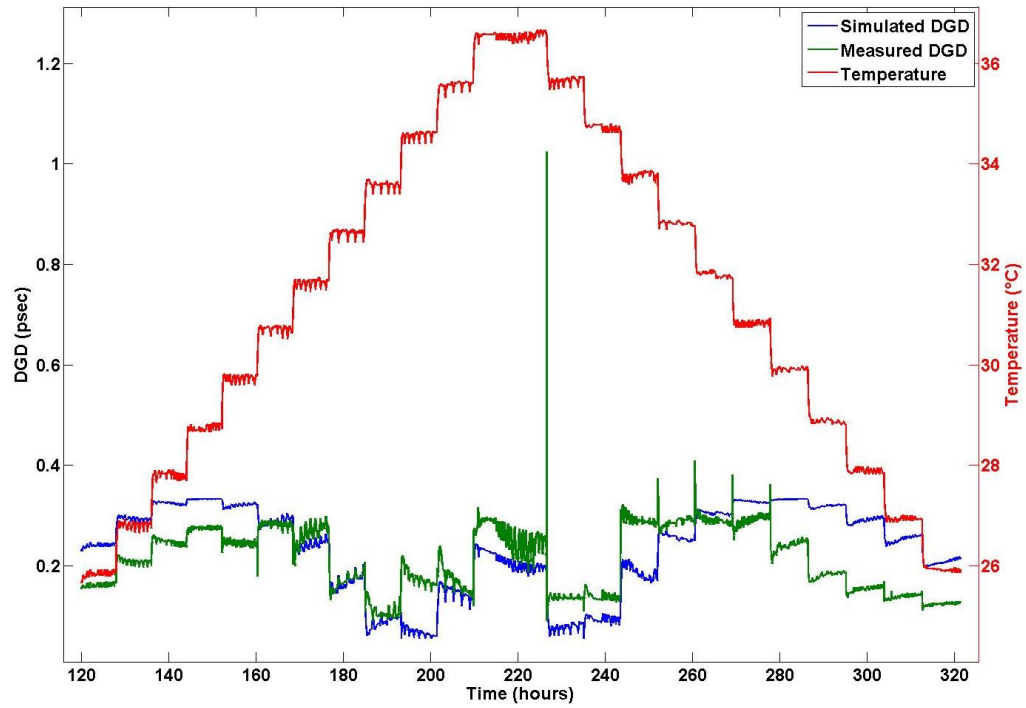


Figure 5.2 DGD (Measured and Simulated) and Temperature versus Time

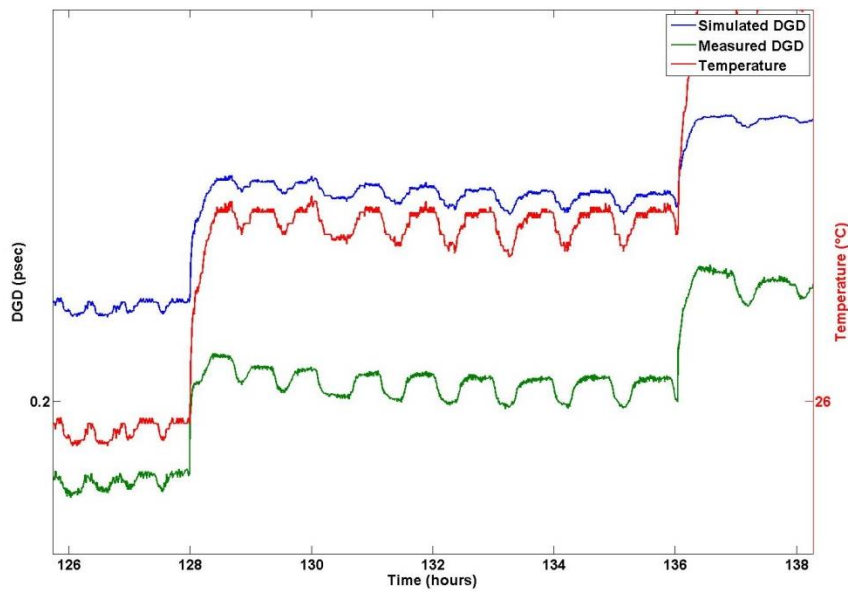


Figure 5.3 A zoomed view on the second heating cycle

5.4 Conclusion

In this thesis we have investigated the behavior of the DGD of a fiber based DCM as a function of temperature and time. Previous studies that did not incorporate the viscoelastic properties of glass (Chapter 2), could not explain the measured time variation of the DGD for fiber-based components even for constant temperature; although they got similar results as shown in the previous chapter. In Chapter 4, we observed a high degree of correlation between the measured DGD and temperature changes over time; and the observed variation of the DGD was further shown to be invariant over periods of several days. Hence, the assumption that repeated measurements of DGD with time describe a Maxwellian distribution [25] is only valid for a system located in an uncontrolled temperature environment.

To demonstrate the relationship between DGD, temperature and time, different mathematical birefringence models were employed in this thesis to simulate the measured data. Simulations showed that the DGD relaxation arises from the viscoelastic property of glass; this is clearly displayed through the high resemblance of curves features between the simulated DGD, measured DGD and measured temperature. Knowledge of the relaxation times of the DGD could be useful in understanding the behavior of buried fiber sections or of highly stable optical links, possibly such as those relevant to quantum communication.

The numerical model of PMD behavior presented in this thesis could be improved through additional knowledge of the material properties of the fiber as well as of manufacturing parameters, such as the tension imparted to the fiber while coiled on the DCM's aluminum drum and the exact length of the fiber in the DCM. More accurate data for the temperature dependence of the volume viscosity of glass would also significantly enhance the model. In this regard, our model of fiber viscoelasticity consisting of a spring and a Voigt element neglected stresses between the core and the cladding glasses. Incorporating these stresses could conceivably further enhance the accuracy of our physical model and might suggest manufacturing techniques for minimizing temperature induced stresses variations that would lead to fibers with reduced temperature sensitivity, improving the DGD stability of high-speed communication links.

Finally, measurements of DGD for standard fibers, coiled on metal spools with different expansion coefficients would as well significantly improve our understanding of the fiber system and the predictive ability of our numerical model. Also, access to a fixed temperature environment would lead to a more uniform temperature distribution over the aluminum body of the DCM when compared to what achieved with discrete temperature control modules.

Appendix A

Matlab code to plot measured data and prepare it for simulation

```

clear all
close all
clc

figure(3)
hold on
figure(4)
hold on
figure(6)
hold on
Temperature=[26:37 37:-1:26];
time_diff_between_files=0;
for i=1:24
    cmd=sprintf ('load
%iconsecutive_readings_for_comparison_with_simulations%i.mat',
i, Temperature(i));
    eval(cmd)
    DGD(i,:)=dgd';
    mean_dgd(i,:)=mean(dgd(25:end)');
    Time(i,:)=T;
    Temp1=mean(Temperature1');
    Temp2=mean(Temp_Upper');
    Temp3=mean(Temperature2');
    Temp4=mean(Temp_Bottom');
    TEMP1(i,:)=mean([Temp1;Temp2;Temp3;Temp4]);%erature1');
    mean_temperature(i,:)=mean(TEMP1(i,25:end)');
    strthere(i,:)=strt;
    if i==1
        figure(3)
        plot(Time(i,:)/3600,DGD(i,:))
        figure(4)
        plot(Time(i,:)/3600,TEMP1(i,:))

        time_axis=[(Time(i,:)+time_diff_between_files)];
        measured_DGD_axis=[DGD(i,:)];
        measured_temperature_axis=[TEMP1(i,:)];
    elseif i==9 %loop added to compensate for timing due to day light
saving
        time_diff_between_files=etime(strthere(i,:),strthere(i-
1,:))+time_diff_between_files+3600;
        figure(3)
        plot((Time(i,:)+time_diff_between_files)/3600,DGD(i,:))
        figure(4)
        plot((Time(i,:)+time_diff_between_files)/3600,TEMP1(i,:))
        adjusted_local_time=(Time(i,:)+time_diff_between_files);
        time_axis=[time_axis adjusted_local_time];
        measured_DGD_axis=[measured_DGD_axis DGD(i,:)];

```

```

        measured_temperature_axis=[measured_temperature_axis TEMP1(i,:)];
    else
        time_diff_between_files=etime(strthere(i,:),strthere(i-
1,:))+time_diff_between_files;%Time(i-1,end)+x;
        figure(3)
        plot((Time(i,:)+time_diff_between_files)/3600,DGD(i,:))
        figure(4)
        plot((Time(i,:)+time_diff_between_files)/3600,TEMP1(i,:))
        adjusted_local_time=(Time(i,:)+time_diff_between_files);
        time_axis=[time_axis adjusted_local_time];
        measured_DGD_axis=[measured_DGD_axis DGD(i,:)];
        measured_temperature_axis=[measured_temperature_axis TEMP1(i,:)];
    end
end
figure(6)
[AX,H1,H2] =
plotyy(time_axis/3600,measured_DGD_axis,time_axis/3600,measured_temperatur
e_axis);
set(get(AX(1),'Ylabel'),'String','DGD (psec)')
    set(get(AX(2),'Ylabel'),'String','Temperature (°C)')
    xlabel('Time (hours)')

clear i j n
sampling_factor=10;
buffer_days=5;
buffer_time=0:mean(diff(time_axis)):buffer_days*3600*24;
buffer_time_size=floor(buffer_days*3600*24/mean(diff(time_axis)))+1;

time_axis=[buffer_time time_axis+buffer_time(1,end)];
measured_temperature_axis=[measured_temperature_axis(1,1)*ones(1,size(buff
er_time,2)) measured_temperature_axis];
measured_DGD_axis=[measured_DGD_axis(1,1)*ones(1,size(buffer_time,2))
measured_DGD_axis];

temperature_slope=diff(measured_temperature_axis)./diff(time_axis);
DGD_slope=diff(measured_DGD_axis)./diff(time_axis);
equally_sampled_time_axis=time_axis(1,1):(time_axis(1,end)-
time_axis(1,1))/sampling_factor/size(time_axis,2):time_axis(1,end);
equally_sampled_temperature_axis(1)=measured_temperature_axis(1);
equally_sampled_measured_DGD_axis(1)=measured_DGD_axis(1);
n=2;
for j=2:size(equally_sampled_time_axis,2)
    for i=n:size(time_axis,2)
        if time_axis(i-1)<equally_sampled_time_axis(j) &&
equally_sampled_time_axis(j)<time_axis(i) ||
j==size(equally_sampled_time_axis,2)

equally_sampled_temperature_axis(j)=measured_temperature_axis(i-
1)+temperature_slope(i-1)*(equally_sampled_time_axis(j)-time_axis(i-1));
        equally_sampled_measured_DGD_axis(j)=measured_DGD_axis(i-
1)+DGD_slope(i-1)*(equally_sampled_time_axis(j)-time_axis(i-1));

```

```

        n=i;
        break
    end
end
end
figure
plot (equally_sampled_time_axis/3600, equally_sampled_temperature_axis)
hold on
plot(time_axis/3600,measured_temperature_axis,'r')
figure(8)
hold on
plotyy(equally_sampled_time_axis/3600,equally_sampled_measured_DGD_axis,eq
ually_sampled_time_axis/3600, equally_sampled_temperature_axis)

save axium_after_Sandy equally_sampled_time_axis
equally_sampled_temperature_axis equally_sampled_measured_DGD_axis
mean_dgd sampling_factor buffer_time_size mean_temperature

```

Appendix B Matlab model

```

close all
clear all
clc
matlabpool
tic
rng('default')

load measured_time_temperature_vectors.mat;
time=equally_sampled_time_axis(1:end);
Temperature=equally_sampled_temperature_axis(1:end);

Length=5000; %Fiber length(meters)
perturbation_length=25; %perturbation length in
meters
Sections_Number=round(Length/perturbation_length); %Number of concatenated
sections (Fiber length/ perturbation length)
R_curvature=8.75e-2; %Radius of curvature of
the coiled fiber
outer_radius=125e-6; %fiber outer radius
mean_ellip=0; %mean ellipticity value
.00120e-12
mean_sec_length=(Length/Sections_Number); %mean section length
sec_length_std=0.01; %section length standard
deviation
n_core=1.44402 ; %core refractive index
n_icladding=1.4388; %cladding refractive
index
lambda=1.55e-6 ; %wave length(meters)
Dlambda=2e-9; %delta wave
length(meters)
r_core=4.1e-6 ; %Core radius(meters)
c=3e8; %Light velocity (m/sec)
alfaclad=9.19e-7 ; %Thermal expansion
coefficient of the cladding
alfacore=5.6e-7 ; %Thermal expansion
coefficient of the core
T_Soft=1065 ; %Softening temperature
of the glass
N=0.17 ; %Poisson's ratio of the
fiber material
p11=0.126 ; %components of the
photoelastic tensor
p12=0.260 ; %components of the
photoelastic tensor
n=mean([n_core,n_icladding]); %mean refractive index
youngmodulus=68e9; %Young modulus
initial_starin= 0.95/(pi*outer_radius^2)/youngmodulus;%Strain applied
while winding the fiber around the spool
Temp0=25; %temperature at which
thermal strain equal zero
K=youngmodulus/(3*(1-2*N)); %bulk modulus

```

```

etav=5e20; %volumr viscosity at
room temperaturae
relaxation_time1=14.3*3600; %assumed relaxation time
in seconds

%% Calculating K1
xy=etav/(3*K*relaxation_time1);
x1=xy/2+sqrt(xy*xy/4-xy);
y1=(1-1/x1)^-1;
if x1<y1
    etav_3k1= 3*y1*K/etav;
else
    etav_3k1= 3*x1*K/etav;
end
relaxation_time= etav/(3*(y1+x1)*K);

%% Calculating the Strain vector versus time
gt=initial_starin-alfaclad*(Temperature-Temp0);
delay=exp(-time/relaxation_time);
CONV=conv(gt,delay);
elastic_strain=gt-etav_3k1*CONV(1:size(gt,2));
figure(7)
hold on
plotyy(time/3600,elastic_strain,time/3600,Temperature)
plot(time/3600,equally_sampled_measured_DGD_axis)

%% removing added time (to minimize simulation time)
time=time(sampling_factor*buffer_time_size:end);
Temperature=Temperature(sampling_factor*buffer_time_size:end);
elastic_strain=elastic_strain(sampling_factor*buffer_time_size:end);
equally_sampled_measured_DGD_axis=equally_sampled_measured_DGD_axis(sampli
ng_factor*buffer_time_size:end);

%% Calculating Fiber Geometry
e=mean_ellip;
rng('default')
section_length=mean_sec_length+(rand(Sections_Number,1)*sec_length_std);

%% calculating propagation paramters
delta=(n_core^2-n_icladding^2)/(2*(n_core^2));

% for Lamda 1
V=2*pi*r_core*sqrt(n_core^2-n_icladding^2)/lambda;
FUN=@(x) (x .* besselj(-1,x) ./ besselj(0,x)) + (sqrt(V^2-x.^2) .*
besselk(-1,sqrt(V^2-x.^2)) ./ besselk(0,sqrt(V^2-x.^2)));
U=fzero(FUN,[0 0.999*V]);
W=sqrt(V^2-U^2);
n_eff=sqrt((2*pi*n_core/lambda)^2-(U/r_core)^2)*lambda/2/pi;

% for Lamda 2

```

```

DV=2*pi*r_core*sqrt(n_core^2-n_icladding^2)/(lambda+Dlambda);
FUN=@(x) (x .* besselj(-1,x) ./ besselj(0,x)) + (sqrt(DV^2-x.^2) .*
besselk(-1,sqrt(DV^2-x.^2)) ./ besselk(0,sqrt(DV^2-x.^2)));
DU=fzero(FUN,[0 0.999*DV]);
DW=sqrt(V^2-DU^2);
Dn_eff=sqrt((2*pi*n_core/(lambda+Dlambda))^2-
(DU/r_core)^2)*(lambda+Dlambda)/2/pi;

Domega=-2*pi*c*Dlambda/(lambda^2);

%% Calculating the birefringence for each section
% for Lamda 1
Biref_total=zeros(1,size(Temperature,2))/0;
Biref_ellip_core=zeros(1,size(Temperature,2))/0;
Biref_bend=(2*pi/lambda)/4*n_core^3*(p11-
p12)*(1+N)*((outer_radius/R_curvature)^2);
Biref_tension_coiled=(2*pi/lambda)*(n_eff^3)/2*(p11-p12)*(1+N)*(2-3*N)/(1-
N)*(outer_radius/R_curvature).*elastic_strain;
Biref_geometrical=(e.^2)*delta^3*W^2/r_core/V^3*(U^2 + (U^2-
W^2)*(besselj(0,U)/besselj(1,U))^2) +
U*W^2*(besselj(0,U)/besselj(1,U))^3);
Biref_ellip_core=(1-U^2/V^2)*(2*pi/lambda)*n^3*(p11-p12)*((alfa clad-
alfacore)*(T_Soft-Temperature)/(1-N^2))*(e./(1+sqrt(1-e)).^2);
for j=1:size(Temperature,2)

Biref_total(:,j)=Biref_bend+Biref_tension_coiled(j)+Biref_geometrical+Biref_ellip_core(j);
end
figure(1)
hold on
plot(Temperature, Biref_ellip_core, 'r')
plot(Temperature, Biref_bend*ones(1,size(Temperature,2)), 'c')
plot(Temperature, Biref_tension_coiled, 'k')
plot(Temperature, Biref_geometrical*ones(1,size(Temperature,2)), 'g')
plot(Temperature, Biref_total(), 'b')

% for Lamda 2
DBiref_total=zeros(1,size(Temperature,2))/0;
DBiref_ellip_core=zeros(1,size(Temperature,2))/0;
DBiref_bend=(2*pi/(lambda+Dlambda))/4*n_core^3*(p11-
p12)*(1+N)*((outer_radius/R_curvature)^2);
DBiref_tension_coiled=(2*pi/(lambda+Dlambda))*(Dn_eff^3)/2*(p11-
p12)*(1+N)*(2-3*N)/(1-N)*(outer_radius/R_curvature).*elastic_strain;
DBiref_geometrical=(e.^2)*delta^3*DW^2/r_core/DV^3*(DU^2 + (DU^2-
DW^2)*(besselj(0,DU)/besselj(1,DU))^2) +
DU*DW^2*(besselj(0,DU)/besselj(1,DU))^3);
DBiref_ellip_core=(1-DU^2/DV^2)*(2*pi/(lambda+Dlambda))*n^3*(p11-
p12)*((alfa clad-alfacore)*(T_Soft-Temperature)/(1-N^2))*(e./(1+sqrt(1-
e)).^2);
for j=1:size(Temperature,2)

```

```

DBiref_total(:,j)=DBiref_bend+DBiref_tension_coiled(j)+DBiref_geometrical+
DBiref_ellip_core(j);
end

%% Generating angles (in Jones space) between consecutive sections
rng(8);
angles=rand(Sections_Number,1)*2*pi;

%% calculating the PMD
clear i
TotalPMD=zeros(1,size(Temperature,2))/0;
parfor j=1:size(Temperature,2)
    Matrix=eye(2,2);
    for i=1:Sections_Number
        Matrix=[cos(angles(i,1)),-
sin(angles(i,1));sin(angles(i,1)),cos(angles(i,1))]*[exp(1i*Biref_total(1,
j)*section_length(i,1)/2) 0; 0 exp(-
1i*Biref_total(1,j)*section_length(i,1)/2)]*[cos(angles(i,1)),sin(angles(i
,1));-sin(angles(i,1)),cos(angles(i,1))]*Matrix;
    end
    DMatrix=eye(2,2);
    for i=1:Sections_Number
        DMatrix=[cos(angles(i,1)),-
sin(angles(i,1));sin(angles(i,1)),cos(angles(i,1))]*[exp(1i*DBiref_total(1
,j)*section_length(i,1)/2) 0; 0 exp(-
1i*DBiref_total(1,j)*section_length(i,1)/2)]*[cos(angles(i,1)),sin(angles(
i,1));-sin(angles(i,1)),cos(angles(i,1))]*DMatrix;
    end
    TotalPMD(j)=abs(sqrt(4*det((DMatrix/Matrix)-eye(2))/Domega));
end
toc

%% plotting data
figure(7)
hold on
plot(Temperature>TotalPMD/1e-12)

figure(8)
hold on
[AX,H1,H2] = plotyy(time/3600,[TotalPMD/1e-
12;equally_sampled_measured_DGD_axis],time/3600,Temperature);
set(get(AX(1),'Ylabel'),'String','DGD (psec)')
set(get(AX(2),'Ylabel'),'String','Temperature (°C)')
xlabel('Time (hours)')

%% Plotting averaged data
i=1;
for index=1:sampling_factor*1000:size(time,2)
    if (index+1000)<size(time,2)-1

```

```
        avearged_simulated_PMD(i)=mean(TotalPMD(index:index+1000));  
        i=i+1;  
    end  
end  
figure(9)  
hold on  
plot(mean_temperature(1:12),mean_dgd(1:12))  
plot(mean_temperature(13:24),mean_dgd(13:24))  
plot(mean_temperature(1:12),avearged_simulated_PMD(1:12)/1e-12)  
plot(mean_temperature(13:24),avearged_simulated_PMD(13:24)/1e-12)  
xlabel('Temperature (°C)')  
ylabel('DGD (psec)')  
  
save workspace  
matlabpool close
```

Bibliography

- [1] C. D. Poole, R. W. Tkach, A. R. Chraplyvy and D. A. Fishman, "Fading in Lightwave Systems Due to Polarization-Mode Dispersion," *Photonics Technology Letters*, vol. 3, no. 1, pp. 68-70, January 1991.
- [2] Amnon Yariv, Pochi Yeh, *Optical Electronics in Modern Communications*, 6th ed., New York: Oxford university press, 2007.
- [3] J.P.Gprdon and H. Kogelnik, "PMD fundamentals: POLarization mode dispersion in optical fiber," *PNAS*, vol. 97, no. 9, pp. 4541-4550, April 2005.
- [4] M. A. Reimer, *Modeling and Simulation of Polarization Mode Dispersion and Polarization Dependent Loss*, 2007.
- [5] P. H. Schönemann, "A Generalized Solution of the Orthogonal Procrustes Problem," *Psychometrika*, vol. 31, no. 1, March, 1966.
- [6] G. W. Scherer, *Relaxatiton in Galass and Composites*, New York: John Wiley & Sons, 1986.
- [7] G. W. Morey, *The Properties of Glass*, 1st ed., Baltimore: The Waverly Press, 1938, p. 302.
- [8] C. J. Phillips, *Glass: The Miracle Maker*, 2nd ed., New York: Pitman Publishing Corporation, 1941, p. 62.
- [9] J. Lyklema and H. Van Olphen, "Terminology and Sumbols in Colloid and Surface Chemistry Part 1.13. Definitions, Terminology and Symbols for Rheological Properties," *Pure and Applied Chemistry (IUPAC)*, vol. 51, pp. 1213 - 1218, 1979.
- [10] J. H. Wary and John T. Neu, "Refractive Index of Several Glasses as a Function of Wavelength and Temperature," *Journal of The Optical Society of America*, vol. 59, no. 6, pp. 774 - 776, June 1969.
- [11] Costantino De Angelis, Andrea Galtarossa, Giovanni Gianello, Franco Matera and Marco Schiano, "Time Evolution of Polarization Mode Dispersion in Long Terrestrial Links," *Journal of Lightwave Thechnology*, vol. 10, no. 5, pp. 552 - 554, May 1992.
- [12] T.Takahashi, T. Imai and M. Aiki, "Time Evolution of Polariazation Mode Dispersion in 120 Km Installed Optical Cable," *Electronics Letters*, vol. 29, no. 18, pp. 1605 - 1606, September 1993.
- [13] John Cameron, Liang Chen, Xiaoyi Bao and John Stears, "Time Evolution of Polarization Mode Dispersion in Optical Fibers," *Photonics Technology Letters*, vol. 10, no. 9, pp. 1265-1267, September 1998.
- [14] Misha Brodsky, Nicholas J. Frigo, Misha Boroditsky and Moshi Tur, "Polarization Mode

- Dispersion of Installed Fibers," *Lightwave Thechnology*, vol. 24, no. 12, pp. 4584-4599, December 2006.
- [15] T. Geisler and P. Kristensen, "Polarization Properties of DCMs: Thermal Variations," in *Optical Fiber Communication Conference*, San Diego, California, 2009.
- [16] M. J. Adams, D. N. Payne and C. M. Ragdale, "Birefringence in optical fibers with elliptical cross-section," *Electronics Letters*, vol. 15, no. 10, pp. 298 -299, May 1979.
- [17] J. D. Love, R. A. Sammut and A. W. Snyder, "Birefringence in elliptically deformed optical fibers," *Electronics Letters*, vol. 15, no. 20, pp. 615 - 616, September 1979.
- [18] R. A. Sammut, "Birefringence in slightly elliptical optical fibers," *Electronics Letters*, vol. 16, no. 19, pp. 728 - 729, September 1980.
- [19] A.W. Snyder, J. Love, in *Optical Waveguide Theory*, New York, Chapman and Hall, 1983, p. 373.
- [20] W. Eickhoff, "Stress-induced single-polarization single-mode fiber," *Optics Letters*, vol. 7, no. 12, pp. 629-631, December 1982.
- [21] R. Ulrich, S. C. Rashleigh and W. Eickhoff, "Bending-induced birefringence in single-mode fibers," *Optics Letters*, vol. 5, no. 6, pp. 273 - 275, June 1980.
- [22] S. C. Rashleigh and R. Ulrich, "High birefringence in tension-coiled single-mode fibers," *Optics Letters*, vol. 5, no. 8, pp. 354 - 356, August 1980.
- [23] C. Chin-Lin, *Foundations for guided-wave optics*, Hoboken: John Wiley & Sons, Inc., 2007.
- [24] Misha Brodsky, Peter Magill and Nicholas J. Frigo, "Polarization-Mode Dispersion of Installed Recent Vintage Fiber as a Parametric Function of Temperature," *Photonics Technology Letters*, vol. 16, no. 1, pp. 209-211, January 2004.
- [25] Alan Eli Willner, S. M. Reza Motaghian Nezam, Lianshan Yan and Michelle C. Hauer, "Monitoring and Control of Polarization-Related Impairments in Optical Fiber Systems," *LIGHTWAVE TECHNOLOGY*, vol. 22, no. 1, pp. 106 - 125, 2004.
- [26] V. Ramaswamy, R. H. Stolen, M. D. Divino and W. Pleibel, "Birefringence in elliptically clad borosilicate single-mode fibers," *Applied Optics*, vol. 18, no. 24, pp. 4080 - 4084, December 1979.
- [27] Andrea Galtarossa and Luca Palmieri, "Measurements of beat length and perturbation length in long single-mode fibers," *Optics Letters*, vol. 25, no. 6, pp. 384 - 386, March 2000.
- [28] P. K. A. Wai and C. R. Menyuk, "Polarization Mode Dispersion, Decorrelation, and Diffusion in Optical Fibers with Randomly Varying Birefringence," *Lightwave Technology*, vol. 14, no. 2,

pp. 148 -157, February 1996.

- [29] Deepak Gupta, Arun Kumar, K. Thyagarajan, "Polarization mode dispersion in single mode optical fibers due to core-ellipticity," *Optics Communications*, vol. 263, no. 1, pp. 36-41, July 2006.